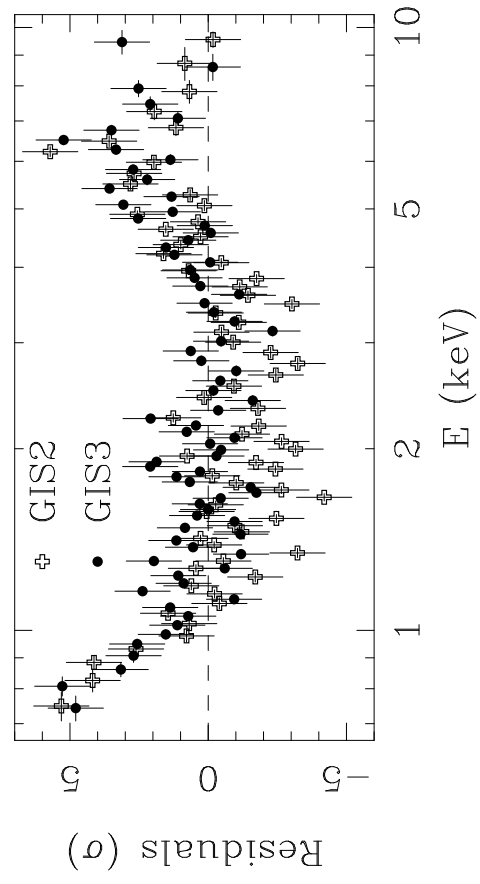
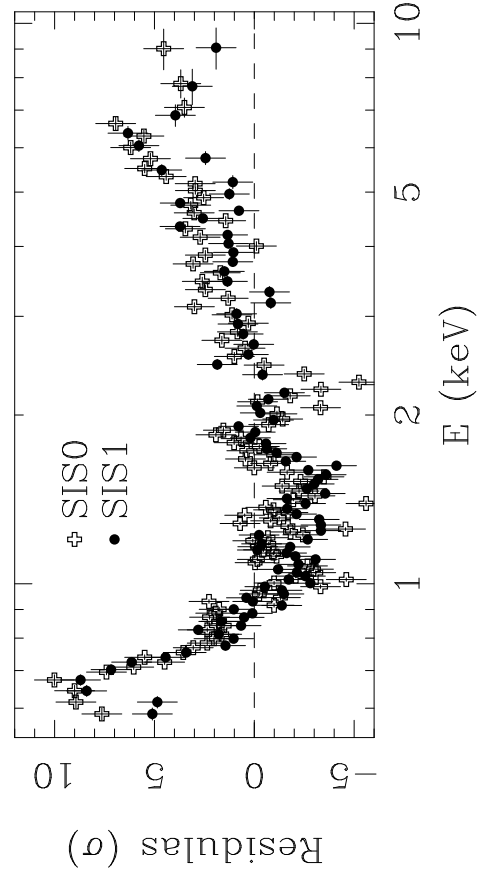
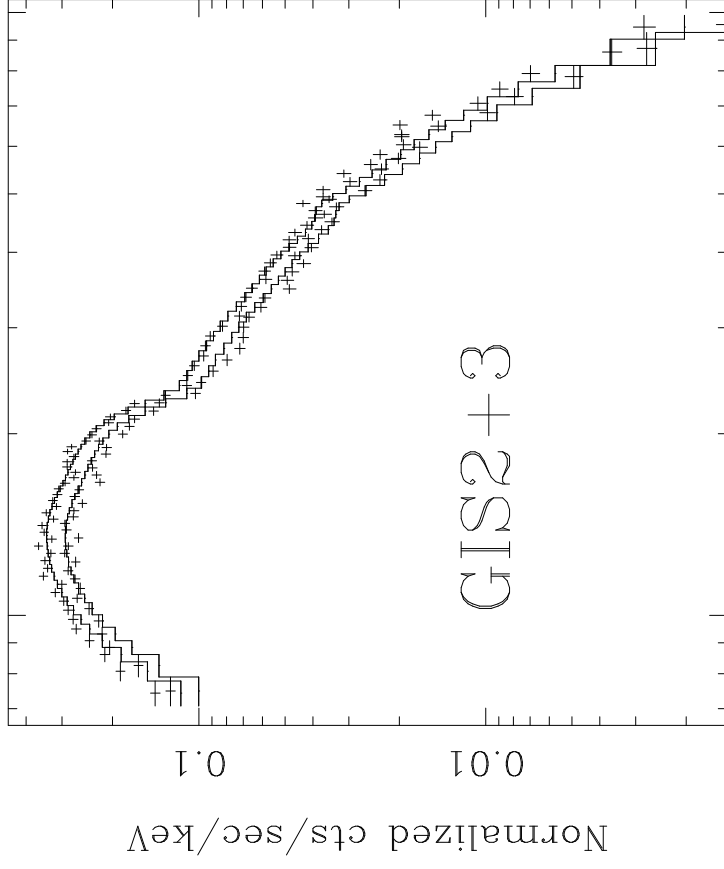
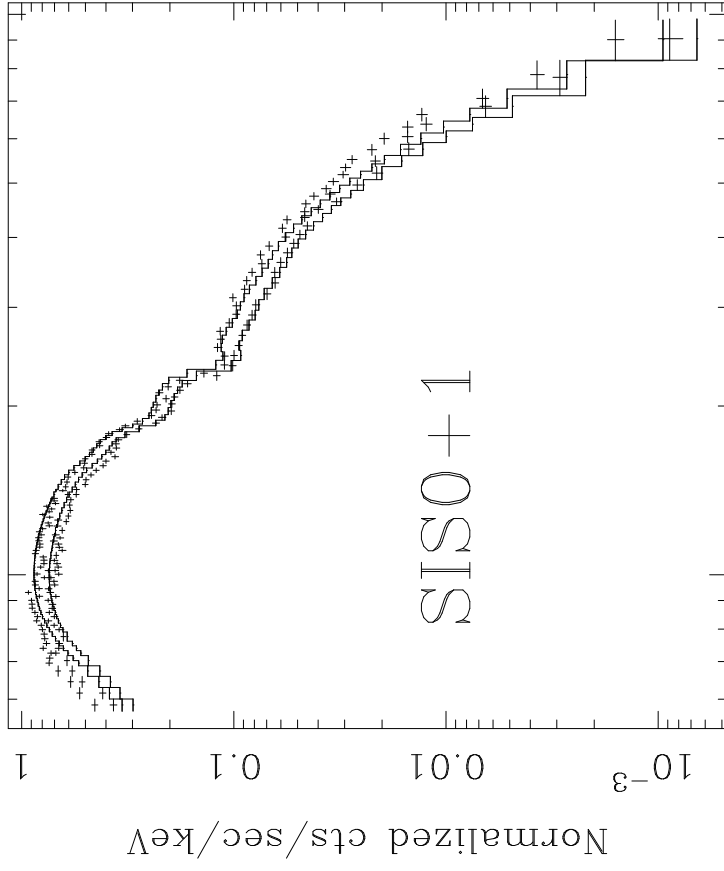
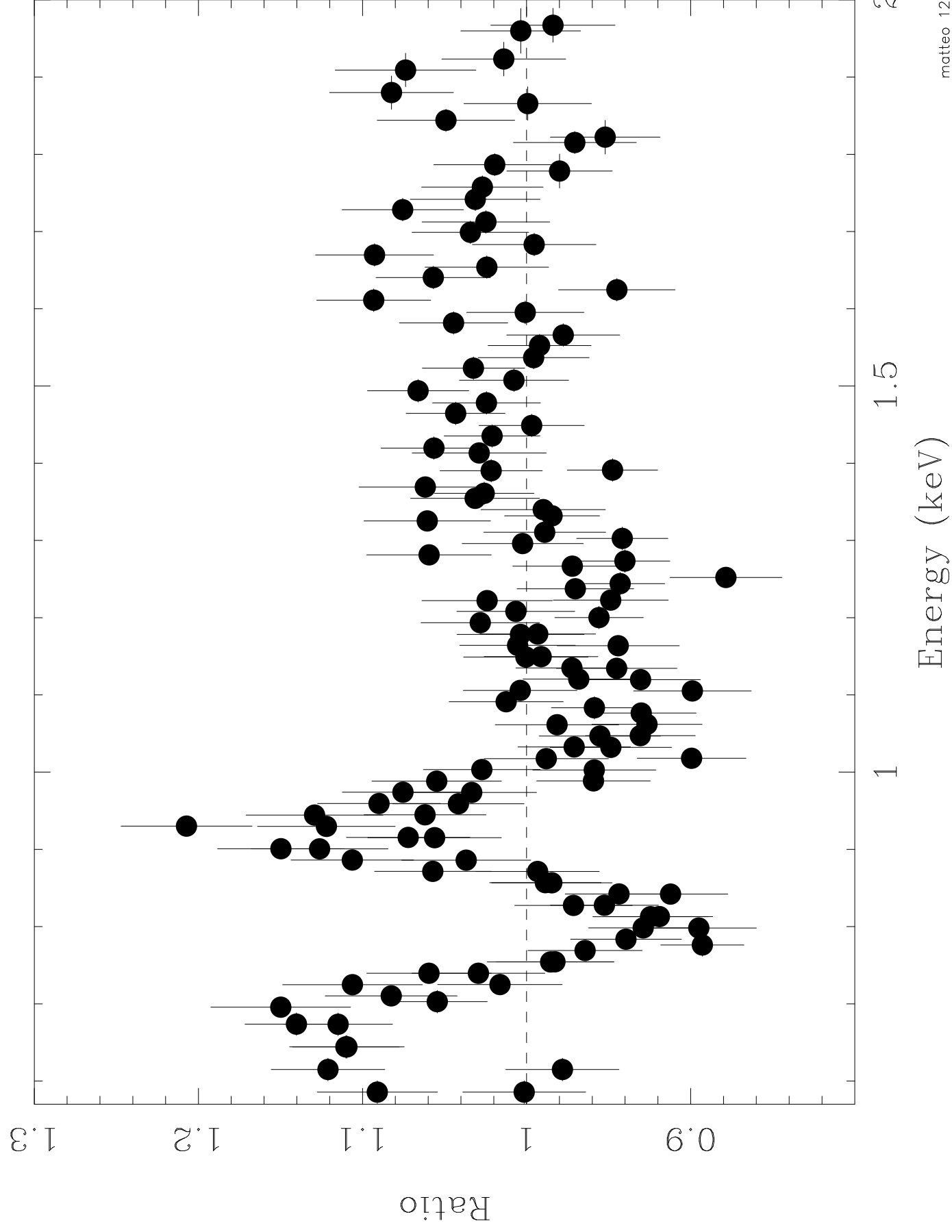
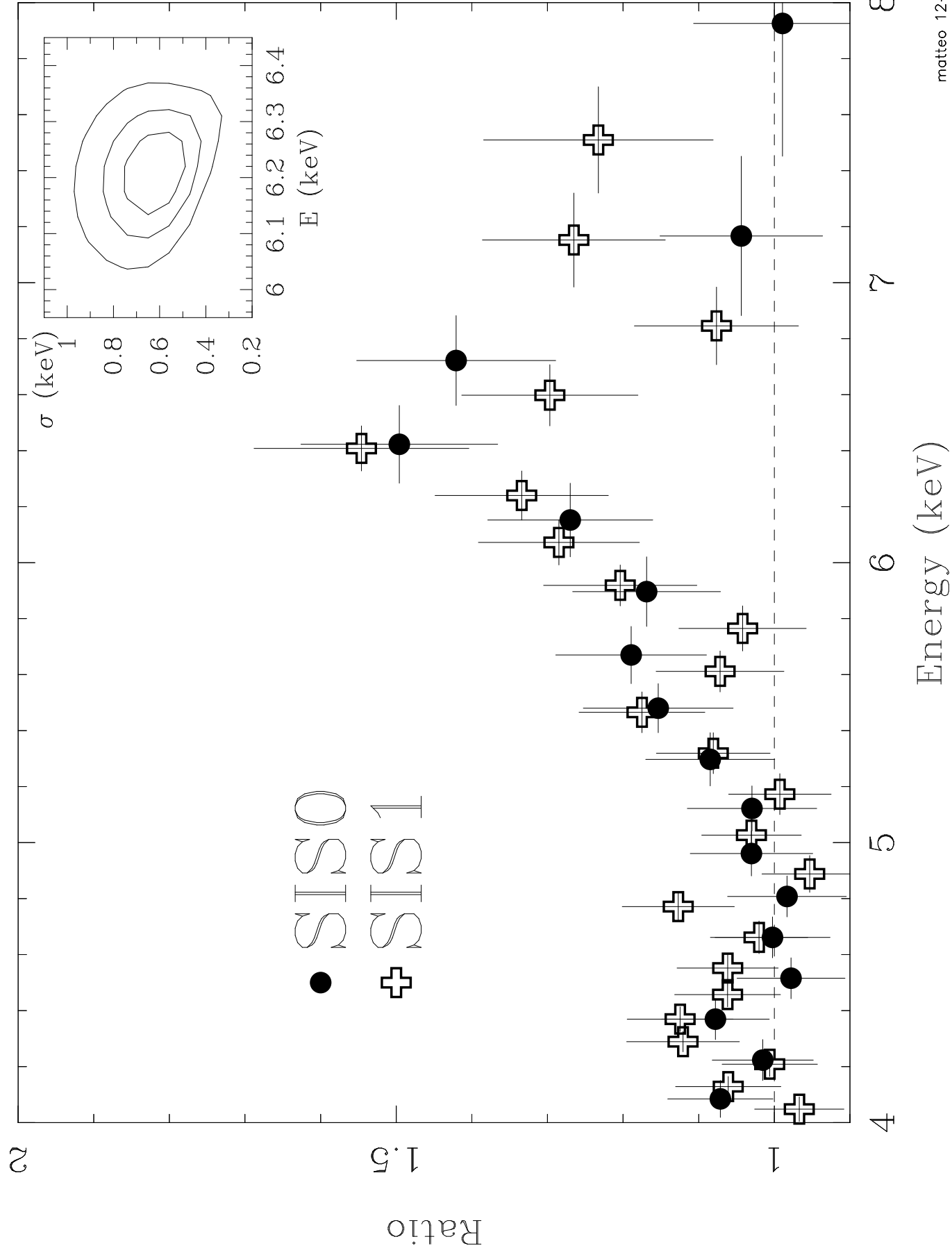
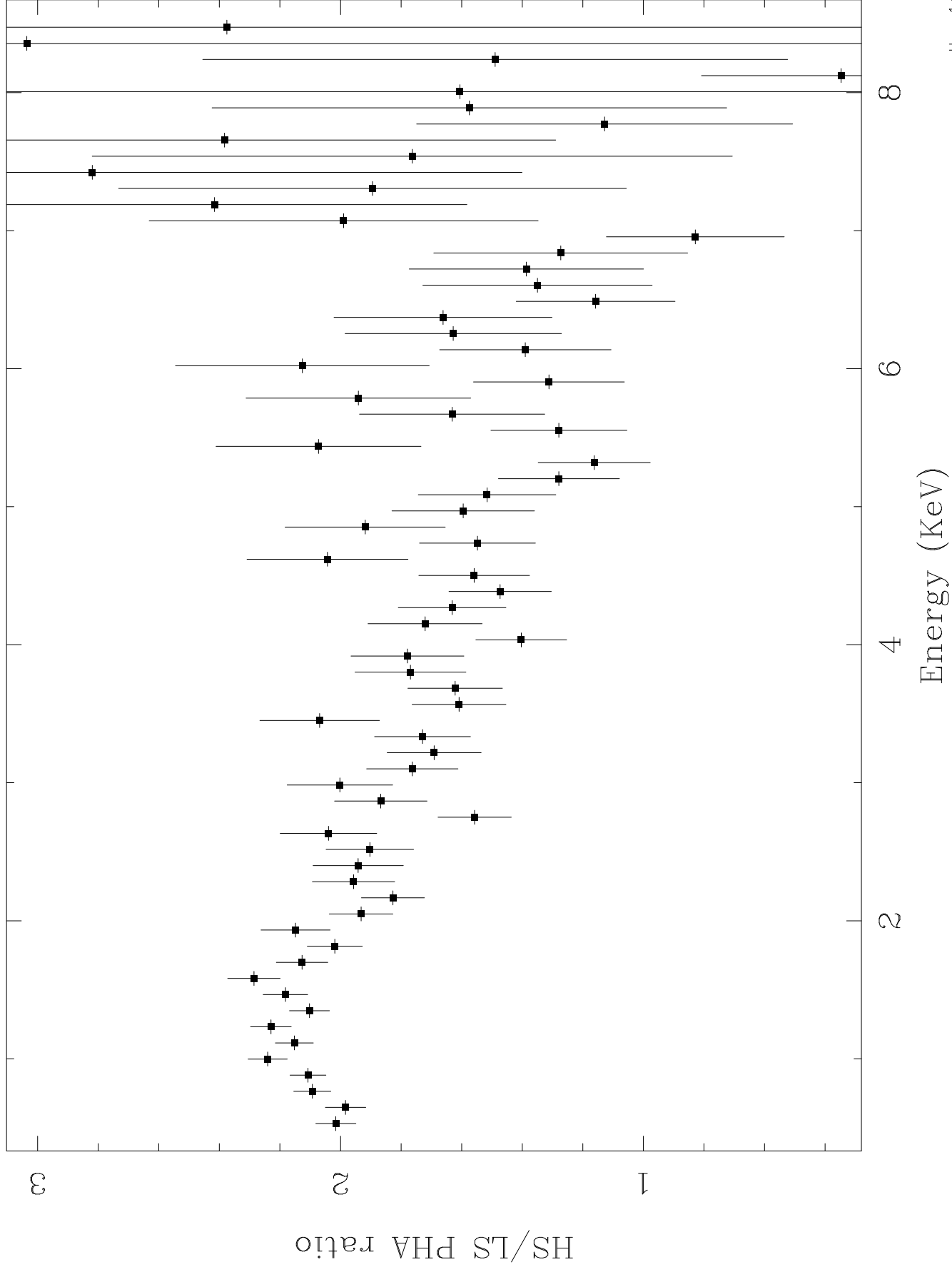


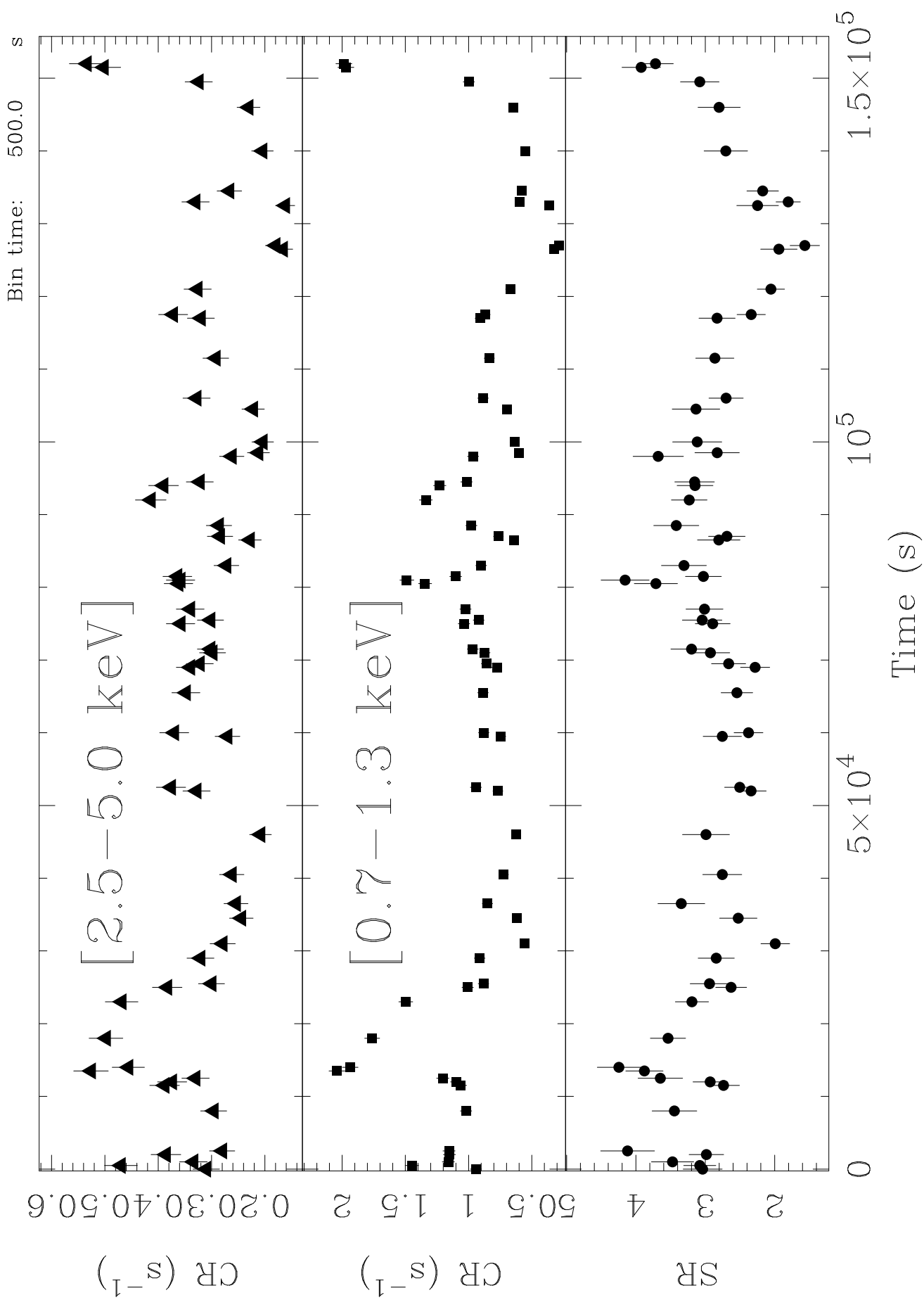
CO = 2.7687E-02, EC = 0.0000E+00, EW = 480.7 , FN=-2.7687E-02, WV= 1.4031E-02  
 CO = 2.8600E-02, EC = 0.0000E+00, EW = 379.4 , FN=-2.8600E-02

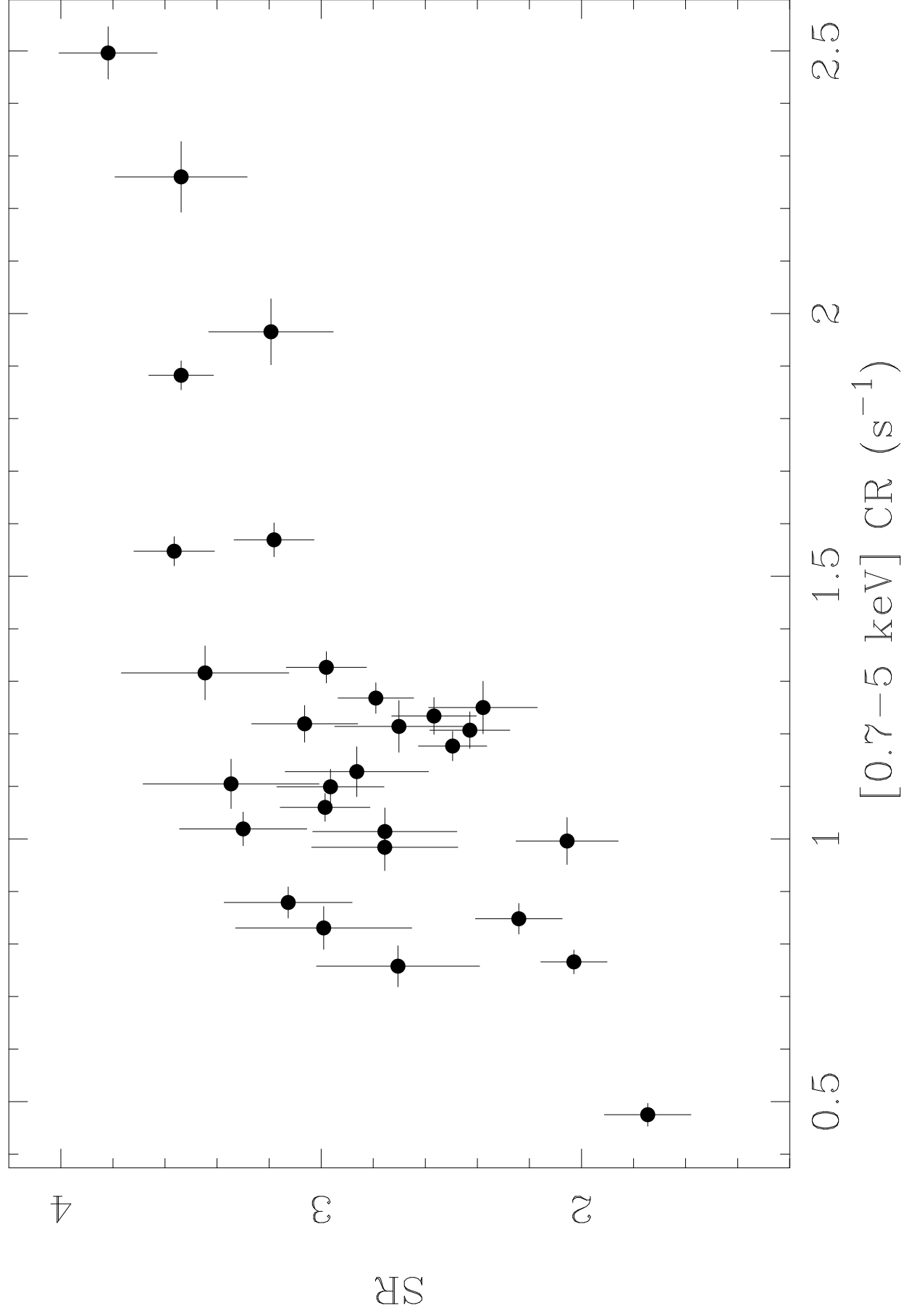




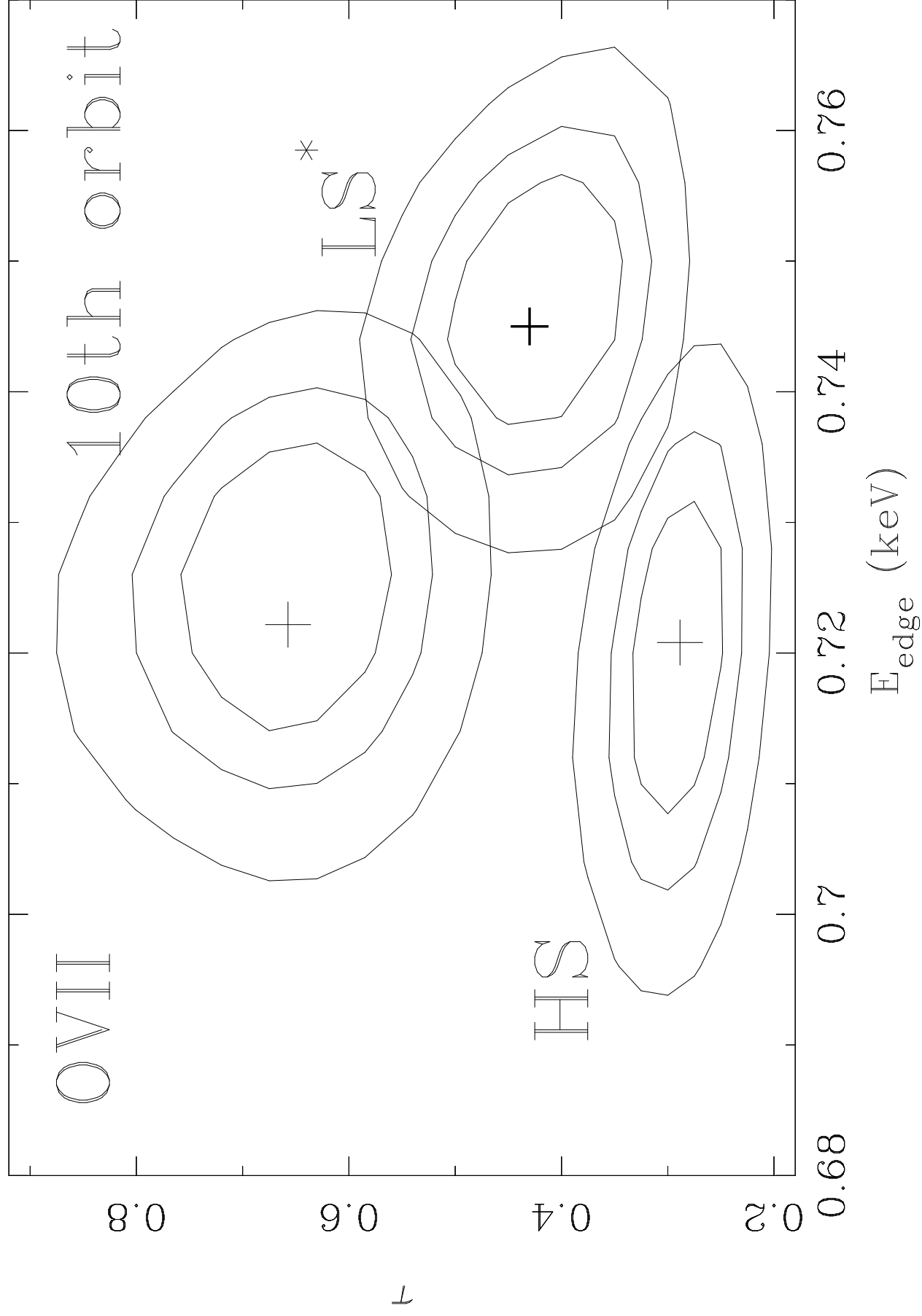


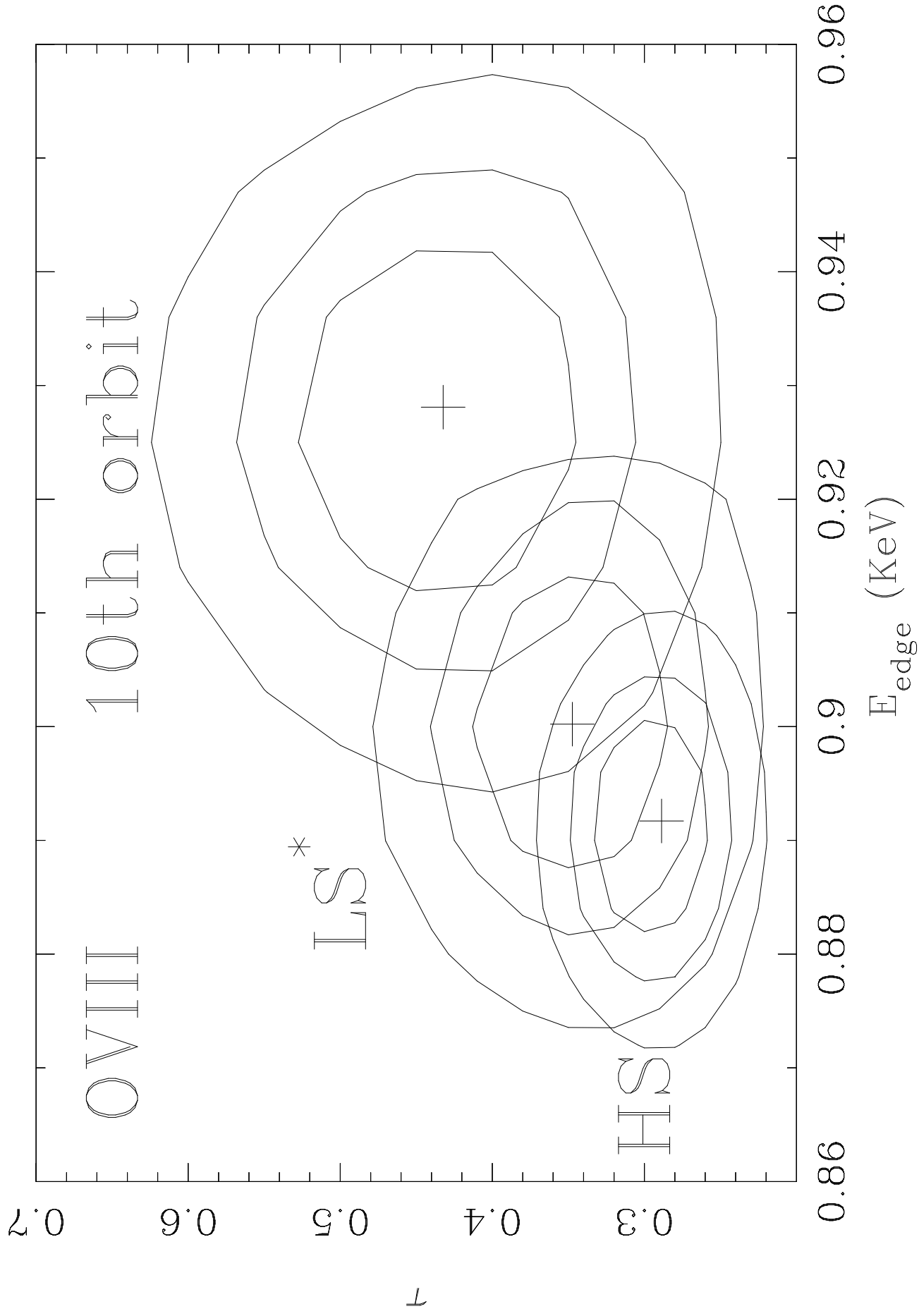


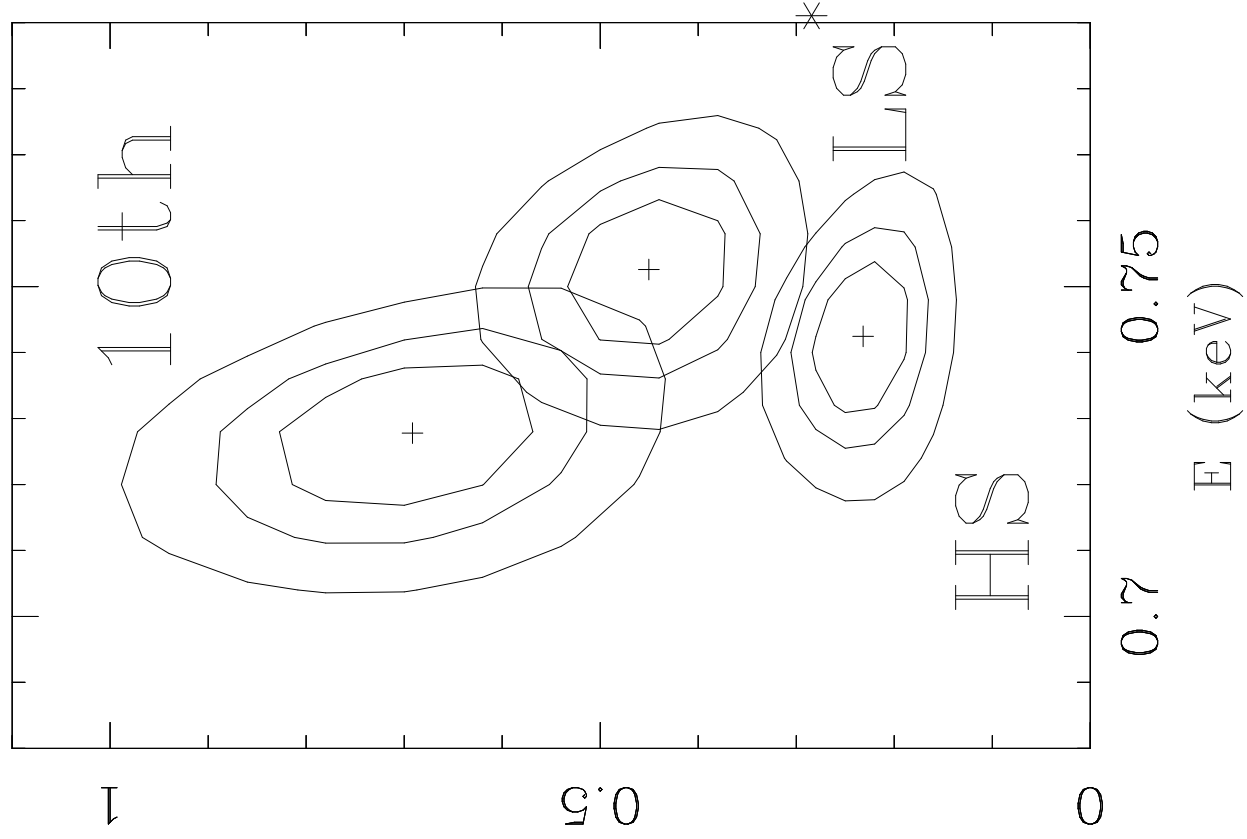
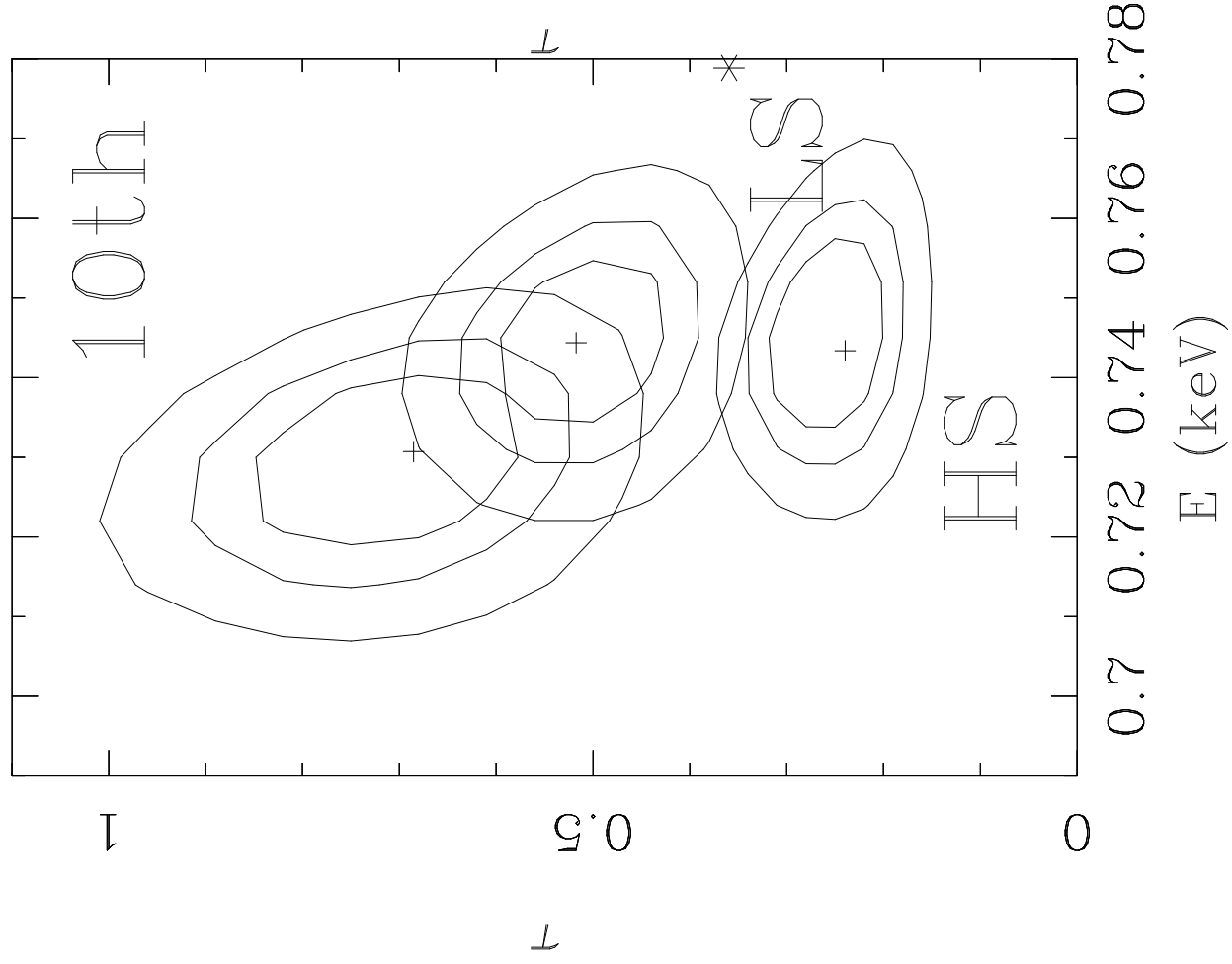












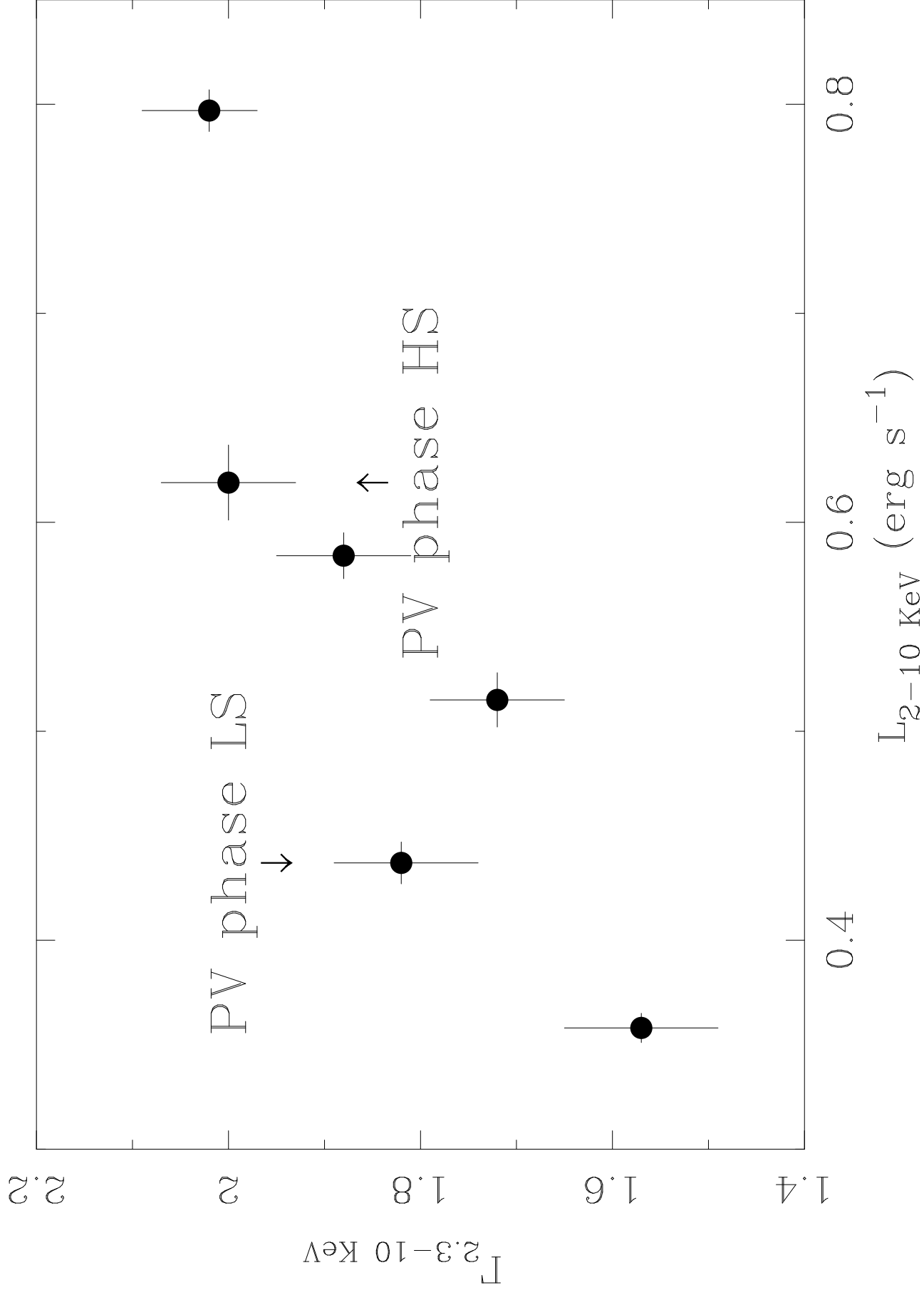


TABLE 2: Best fit parameters for low energy ( $E \leq 5$  keV) SIS0+1 spectral fits (PL = power-law, BB = blackbody, ED = absorption edge, GA = gaussian line, BREMS = bremsstrahlung, DISKBB = accretion disk multitemperature blackbody)

Model	$F_{se}^\dagger$	$E_{OVII}$ (keV)	$\tau_{OVII}$	$E_{OVIII}$ (keV)	$\tau_{OVIII}$	$E_3$ (keV)	$\tau_3$ or
PL + BB	$0.61^{+0.11}_{-0.10}$	...	...	...	...	...	
PL + BB + 1 ED	$0.71^{+0.08}_{-0.09}$	$0.752 \pm 0.016$	$0.23 \pm 0.04$	...	...	...	
PL + BB + 2 EDs	$0.94^{+0.12}_{-0.09}$	$0.74 \pm 0.01$	$0.36 \pm 0.04$	$0.92 \pm 0.02$	$0.22 \pm 0.04$	...	
PL + BB + 3 EDs (E) <sup>‡</sup>	$1.1 \pm 0.6$	$0.733^{+0.014}_{-0.095}$	$0.35^{+0.04}_{-0.13}$	$0.86^{+0.04}_{-0.03}$	$0.12^{+0.05}_{-0.06}$	$0.96 \pm 0.02$	0.
PL + BB + 2EDs + GA (L) <sup>‡</sup>	$1.00^{+0.15}_{-0.13}$	$0.734 \pm 0.013$	$0.35^{+0.04}_{-0.03}$	$0.89 \pm 0.02$	$0.31^{+0.05}_{-0.06}$	$0.94 \pm 0.02$	
PL + BREMS + 2ED + GA	$1.8^{+1.2}_{-1.0}$	$0.737 \pm 0.013$	$0.29 \pm 0.05$	$0.90 \pm 0.02$	$0.22^{+0.06}_{-0.04}$	$0.93^{+0.07}_{-0.02}$	
PL + DISKBB + 2ED + GA	$1.2^{+1.1}_{-0.6}$	$0.734 \pm 0.012$	$0.31^{+0.05}_{-0.06}$	$0.90 \pm 0.02$	$0.26 \pm 0.05$	$0.93 \pm 0.02$	
PL + PL + 2ED + GA	$3.2^{+0.9}_{-0.8}$	$0.747^{+0.014}_{-0.016}$	$0.21 \pm 0.06$	$0.92^{+0.050}_{-0.013}$	$0.15^{+0.06}_{-0.04}$	$0.94 \pm 0.10$	

<sup>†</sup>flux of the soft excess component in the [0.4-2 keV] band expressed in units of  $10^{-11} \text{ erg s}^{-1} \text{ cm}^{-2}$

<sup>‡</sup>referred to as “Model E” and “Model L” in text respectively

TABLE 3: Best-fit parameters and  $\chi^2$  values for High energy ( $E \geq 2.3$  keV) SIS0+1 and GIS2+3 simultaneous spectral fits

Model	$\Gamma$	$E_1$ (keV)	$\sigma_1$ (eV)	$EW_1$ (eV)	$E_2$ (keV)	$EW_2$ (eV)	$E_3$ (keV)	$EW_3$ (keV)	$\chi^2/\nu$
SIS0+1									
PL + 1GA	$1.84 \pm 0.06$	$6.3 \pm 0.2$	$0.5^{+0.3}_{-0.2}$	$350^{+170}_{-150}$	...	...	...	...	55.5
PL + 2GA	$1.85 \pm 0.07$	$6.2 \pm 0.2$	$0.7 \pm 0.4$	$320 \pm 190$	$6.44^{+0.05}_{-0.24}$	$40 \pm 30$	...	...	54.0
PL + 3GA	$1.84^{+0.07}_{-0.04}$	$6.3 \pm 0.2$	$0.5^{+0.4}_{-0.2}$	$270^{+190}_{-120}$	$6.44^{+0.05}_{-0.26}$	$40 \pm 30$	$5.4^{+0.7}_{-0.5}$	$21 \pm 17$	54.0
GIS2+3									
PL + 1GA	$1.89^{+0.03}_{-0.06}$	$6.0 \pm 0.3$	$0.9 \pm 0.6$	$500^{+600}_{-300}$	...	...	...	...	60.0
PL + 2GA	$1.85 \pm 0.05$	$6.3 \pm 0.2$	$0.5(fixed)$	$250 \pm 80$	...	...	$5.5 \pm 0.7$	$< 60$	61.0
PL + 3GA	$1.83^{+0.05}_{-0.03}$	$6.41 \pm 0.08$	$0(fixed)$	$160^{+50}_{-40}$	...	...	$5.62 \pm 0.12$	$60^{+30}_{-20}$	60.0

TABLE 5: Log of temporal subdivision of the observation, SIS1 count rate (mean count rate = 1.11 cts/s), OVII and OVIII absorption edges optical depths and [2–10 keV] photon index in the E model case

Orbit	$t_{start} - t_{end}$ (Ks) <sup>†</sup>	Exposure (s)	CR s <sup>-1</sup>	$\tau_{OVII}$	$\tau_{OVIII}$	$\Gamma_{2.3-10 \text{ keV}}$
1	0-20	10448	1.60	$0.28 \pm 0.08$	$0.16 \pm 0.07$	$2.08 \pm 0.09$
2	20-60	15105	0.90	$0.37 \pm 0.09$	$0.17 \pm 0.08$	$1.68^{+0.05}_{-0.06}$
3	60-64	1382	1.48	$< 0.57$	$< 0.35$	$2.0 \pm 0.2$
4	64-75	5291	1.14	$0.48^{+0.15}_{-0.11}$	$0.22 \pm 0.12$	$1.76 \pm 0.09$
5	75-81.5	3521	1.28	$0.23^{+0.16}_{-0.15}$	$0.18 \pm 0.14$	$1.83^{+0.54}_{-0.12}$
6	81.5-88.5	3884	0.96	$< 0.36$	$< 0.26$	$1.82 \pm 0.11$
7	88.5-95	3231	1.22	$0.30^{+0.22}_{-0.19}$	$0.16 \pm 0.16$	$1.98^{+0.16}_{-0.13}$
8	95-108	5281	0.81	$0.32 \pm 0.16$	$< 0.18$	$1.81 \pm 0.03$
9	108-115	2499	1.31	$0.34 \pm 0.22$	$0.21^{+0.17}_{-0.16}$	$2.1 \pm 0.3$
10	115-140	10289	0.66	$0.63^{+0.14}_{-0.13}$	$< 0.16$	$1.6 \pm 0.4$
11	140-155	6646	1.50	$0.35 \pm 0.11$	$< 0.13$	$1.91^{+0.07}_{-0.06}$

<sup>†</sup>times are calculated from the start of the observation

TABLE 6: Best-fit parameters for the low energy spectral features in SIS0+1 spectra of time-resolved phases

Phase	$E_{OVII}$ (keV)	$\tau_{OVII}$	$E_{OVIII}$ (keV)	$\tau_{OVIII}$	$E_3$ (keV)	$\tau_3$ or $EW_3$ (eV)	$\chi^2_\nu$
Model L							
High State	$0.726 \pm 0.012$	$0.29 \pm 0.07$	$0.88 \pm 0.04$	$0.30 \pm 0.06$	$0.94^{+0.02}_{-0.06}$	$8^{+9}_{-6}$	1.06
Low State	$0.739^{+0.013}_{-0.008}$	$0.44^{+0.08}_{-0.06}$	$0.90^{+0.05}_{-0.02}$	$0.31^{+0.09}_{-0.11}$	$0.93^{+0.02}_{-0.03}$	$< 14$	1.06
10th orbit	$0.722 \pm 0.017$	$0.66 \pm 0.12$	$0.91^{+0.02}_{-0.03}$	$0.44 \pm 0.10$	$0.94 \pm 0.08$	$5^\dagger$	1.01
Low State*	$0.743 \pm 0.013$	$0.39^{+0.09}_{-0.10}$	$0.87 \pm 0.04$	$0.34^{+0.10}_{-0.17}$	$0.90^{+0.02}_{-0.05}$	$16^{+10}_{-8}$	0.99
Model E							
High State	$0.723 \pm 0.013$	$0.29^{+0.06}_{-0.05}$	$0.86^\dagger$	$0.14 \pm 0.07$	$0.96 \pm 0.03$	$0.14 \pm 0.05$	1.06
Low State	$0.738^{+0.015}_{-0.007}$	$0.45 \pm 0.08$	$0.86^\dagger$	$< 0.13$	$0.945^{+0.02}_{-0.03}$	$0.21^{+0.09}_{-0.05}$	1.06
10th orbit	$0.722^{+0.017}_{-0.010}$	$0.66 \pm 0.12$	$0.86^\dagger$	$< 0.17$	$0.96^{+0.01}_{-0.05}$	$0.38^{+0.11}_{-0.14}$	1.01
Low State*	$0.746^{+0.012}_{-0.013}$	$0.42^{+0.11}_{-0.12}$	$0.86^\dagger$	$< 0.20$	$0.94 \pm 0.03$	$0.21^{+0.09}_{-0.08}$	0.96

$^\dagger$  unconstrained



TABLE 1: - Good time interval selection criteria

SIS0+1	GIS2+3
SAA.eq.0	
T_SAA.gt.60	
BR_EARTH.gt.20	
ELV_MIN.gt.5	
T_DY_NT.gt.5	
COR_MIN.gt.6	COR_MIN.gt.7
SX_PIXLY.lt.400 <sup>†</sup>	GZ_L1.gt.0 <sup>‡</sup>
<sup>†</sup> X=0,1, Y=1,3	
<sup>‡</sup> Z=2,3	

SAA = South Atlantic Anomaly (0 = passage excluded)

T\_SAA = Time after passage through SAA (in s)

BR\_EARTH = Angle between pointing direction and Earth's terminator (in degrees)

ELV\_MIN = Angle between pointing direction and Earth's limb (in degrees)

T\_DY\_NT = Time after day/night transition (in s)

COR\_MIN = Minimum cut-off rigidity allowed (in GeV/c)

SX\_PIXLY = Maximum number of counts in chip Y of detector SISX

GX\_L1 = GIS2 and GIS3 discriminator

TABLE 7: Best-fit parameters for SIS0+1 and GIS2+3 simultaneous high energy fits on AO2 data quartiles with constant direct vs. reflected normalizations ratio (quartile's definition in text, in brackets the [2–10 keV] luminosity in units  $10^{42} \text{ erg s}^{-1}$ )

Phase	$\Gamma_{2.3-10 \text{ keV}}$	$E_{line}^{Fe} (keV)^{\ddagger}$	$\sigma_{line}^{Fe} (keV)^{\ddagger}$	$EW_{line}^{Fe} (eV)^{\ddagger}$	$\Gamma_{5-10 \text{ keV}}/\Gamma_{2.3-5 \text{ keV}}$	$\chi^2/\text{d.o.f.}$	F-test
1st quartile (0.33)	$1.57 \pm 0.08$	$6.28 \pm 0.14$	$0.20^{+0.12}_{-0.20}$	$250^{+90}_{-100}$	$1.19 \pm 0.19$	295/265	2.4
2nd quartile (0.56)	$1.72 \pm 0.07$	$6.58 \pm 0.14$	$0.08^{+0.17}_{-0.08}$	$180^{+100}_{-90}$	$1.08^{+0.16}_{-0.20}$	299/294	0.1
3rd quartile (0.70)	$1.88 \pm 0.07$	$6.17^{+0.13}_{-0.46}$	$0.13^{+0.69}_{-0.13}$	$200 \pm 90$	$0.93^{+0.15}_{-0.18}$	301/344	0.3
4th quartile (1.13)	$2.02^{+0.07}_{-0.05}$	$6.30 \pm 0.10$	$0.4^{+0.5}_{-0.3}$	$270 \pm 120$	$0.88^{+0.09}_{-0.13}$	578/581	2.5

<sup>†</sup> the quoted F-test is calculated after allowing the  $\Omega/2\pi$  parameter to float in the reflection model. The resulting best-fit values for this parameter are listed in the adjacent column

<sup>‡</sup> $E$  and  $\sigma$  are referred to the main component of the emission complex; the  $EW$  instead is referred to the complex as a whole

TABLE 8: Best-fit parameters for SIS0+1 and GIS2+3 simultaneous high energy fits on AO2 data quartiles with reflected component normalization inversely correlated with total flux

Phase	$\Gamma_{2.3-10 \text{ keV}}$	$E_{line}^{Fe} \text{ (keV)}^{\ddagger}$	$EW_{line}^{Fe} \text{ (eV)}^{\ddagger}$	$\chi^2/\text{d.o.f.}$	$\Omega/2\pi \text{ (fixed)}$
1st quartile	$1.66 \pm 0.09$	$6.0 \pm 0.5$	$100^{+130}_{-100}$	288/277	1.72
2nd quartile	$1.79^{+0.22}_{-0.10}$	$6.6 \pm 0.4$	$110^{+180}_{-110}$	290/277	1.2
3rd quartile	$1.88 \pm 0.07$	$6.2 \pm 0.2$	$200 \pm 90$	322/277	1
4th quartile	$2.05^{+0.09}_{-0.06}$	$5.8 \pm 0.5$	$150 \pm 100$	290/277	0.77

$^{\ddagger}$ line parameters refers to the main component of the emission complex

TABLE 4: Best-fit parameters for the line emission from a relativistic accretion disk model

$q$	$R_i/R_S$	$R_o/R_S$	$\theta$	$EW$ (eV)	$\chi^2/\text{d.o.f.}$
$E_\alpha \equiv 6.4 \text{ keV}$ (cold disk)					
$-1^\dagger$	$9_{-6}^{+\infty}$	$28_{-5}^{+7}$	$25_{-2}^{+3}$	$270 \pm 40$	1157/1230
$-3^\dagger$	$10_{-4}^{+7}$	$34_{-9}^{+\infty}$	$28_{-6}^{+4}$	$270_{-60}^{+30}$	1157/1230
$-2 \pm 3$	$10^\dagger$	$30^\dagger$	$27 \pm 4$	$270 \pm 50$	1157/1230
$E_\alpha \equiv 6.7 \text{ keV}$ (ionized disk)					
$-3^\dagger$	$7 \pm 3$	$5000^\ddagger$	$10_{-10}^{+6}$	$260_{-50}^{+40}$	1157/1230
$-2.9 \pm 0.2$	$8^\dagger$	$5000^\dagger$	$10_{-10}^{+6}$	$260 \pm 50$	1157/1230

$^\dagger$  fixed

$^\ddagger$  unconstrained

Spectral Variability and iron line emission in the ASCA Observations  
of the Seyfert 1 Galaxy NGC4051

Matteo GUAINAZZI<sup>1,2</sup>, Tatehiro MIHARA<sup>2</sup>,  
Chiko OTANI<sup>2</sup> & Masaru MATSUOKA<sup>2</sup>

<sup>1</sup>*Istituto di Fisica, Unità G.I.F.C.O./C.N.R.,  
Via Archirafi 36, I-90123, Palermo*

<sup>2</sup>*The Institute of Physical and Chemical Research,  
2-1 Hirosawa, Wako, Saitama 350-01, Japan*

Send correspondence to:  
Matteo Guainazzi  
SAX Scientific Data Center  
c/o Nuova Telespazio  
Via Corcolle 19  
I-00131 Roma Italy  
e-mail: [matteo@napa.sdc.asi.it](mailto:matteo@napa.sdc.asi.it)

## Abstract

We present the results of an extensive analysis of the *ASCA* AO2 observation of the Seyfert 1 galaxy NGC4051. The target exhibits broadband [0.5–10 keV] variability by a factor  $\sim 8$  on time scales  $\sim 10^4$  s, with a typical doubling time  $\sim 500$  s. The spectrum is characterized by a strong emission excess over the extrapolated power law at energies  $E \leq 1$  keV. Absorption edges due to ionized oxygen species OVII and OVIII are detected together with an emission-like feature at  $E \sim 0.93$  keV. The OVII edge undergoes significant variability on a timescale as low as  $\sim 10^4$  s, whilst no contemporary variability of the OVIII feature is detected. Typical variability time scales place constraints on the location and the density of the absorbing matter. In the self-consistent hypothesis of a high energy ( $E \geq 2.3$  keV) power law reflected by an infinite plane-parallel cold slab, a photon index change ( $\Delta\Gamma = 0.4$ ) has also been observed; a natural explanation can be found in the framework of non-thermal Comptonization models. The iron line is redshifted (centroid energy  $E \sim 6.1$  keV) and broad ( $\sigma > 0.2$  keV); multi-component structure is suggestive of emission from a relativistic accretion disk; however if the disk is not ionized a contribution by a molecular torus or an iron overabundance by a factor  $\sim 1.5$  are required.

**Key words:** Galaxies:individual (NGC4051) - Galaxies: Seyfert - Galaxies: X-rays

## 1 Introduction

NGC4051 is a nearby ( $z = 0.0023$ ) Seyfert 1 galaxy well known as a rapidly variable X-ray source. It was extensively observed in the past decade and both its spectral features and its variability deserved great attention. An emission excess above the extrapolation of a simple power law was discovered by the *Einstein* (Urry *et al.* 1989) and *EXOSAT* (Lawrence *et al.* 1985) experiments in the soft X-ray band. Recent analysis of two pointed *ROSAT* observations indicated the presence of a strong absorption feature at energy  $\sim 0.85$  keV (McHardy *et al.* 1995); it was interpreted as a blending of the photoionization absorption edges of OVII and OVIII. Similar features have been commonly discovered in the *ROSAT* spectra of Seyfert 1 galaxies and explained as due to the presence of highly ionized matter surrounding the central source (the so called “warm absorber” model); they have been confirmed by several *ASCA* targets (among the others MCG-6-30-15, Fabian *et al.* 1994, NGC 3783, George, Turner & Netzer 1993, NGC3227, Ptak *et al.* 1994, NGC5548 and Mrk841, Otani 1996). McHardy *et al.* (1995) calculated self-consistently spectra emitted by matter in photoionization equilibrium with the ionizing continuum, assuming a spherical shell geometry and uniform density; they yielded a value for the ionization parameter  $\xi \sim 300$  and a column density  $N_{warm} \sim 8 \times 10^{22} \text{ cm}^{-2}$ , with an intrinsic energy index  $\simeq 1.19$ .

At higher energy, there was also much evidence of deviation from the simple power law trend. *Ginga* data have been widely analyzed and many different models were claimed to be the best explanation for the observed spectra. Matsuoka *et al.* (1990) supported an interpretation in terms of a partially covered power law with solar abundance or a reflection model or a thermal bremsstrahlung and a power law, whilst Kunieda *et*

*al.* (1992) favoured reprocessing by cold blobs. The detection of an iron K-fluorescence line by neutral or mildly ionized matter provided further support to the hypothesis of nuclear radiation reprocessing.

NGC4051 was observed by the *ASCA* satellite during the Performance Verification phase (PV hereafter). The source fell into one of the SIS1 inter-chip gaps during it. The relevant analysis was published by Mihara *et al.* (1994) (hereafter Paper I) and their main conclusions can be summarized as follows. The unprecedented combination of energy resolution and broadband coverage allowed to discover two distinct absorption edges at energies  $E_1 \simeq 0.74 \text{ keV}$  and  $E \simeq 0.92 \text{ keV}$ ; they were interpreted as due to highly ionized oxygen species OVII and OVIII, although the energy of the latter was blueshifted ( $\sim 6\%$ ). That gave the first direct measurement of warm absorbing gas in NGC4051. A power law modified by a warm absorber could partly explain the apparent soft excess, but the adding of a further thermal component with  $kT \sim 0.1 \text{ keV}$  was required to remove it completely. The best-fit underlying power-law photon index was  $\simeq 1.88$ . A narrow emission line at energy consistent with K-fluorescence by neutral or mildly ionized iron ( $E \simeq 6.45 \text{ keV}$ ) was also detected with an upper limit on the FWHM of  $\sim 460 \text{ eV}$  and equivalent width  $EW \sim 170 \text{ eV}$ .

In this paper we report the results of an extensive analysis of a second *ASCA* observation performed during the AO2 phase, with a much longer integration time than the PV phase. Timing and spectral analysis and short term ( $\leq 2$  days) variability will be mainly addressed and comparison with the PV phase results will be quoted only in such a framework. In §2 data reduction methods and criteria are presented. In §3 we will discuss briefly the broadband variability and characterize it from a statistical point of view. §4 will deal with the spectral analysis of the AO2 data, while in §5 the variability of the main grand spectral features observed will be studied in detail. §6 will be devoted to a discussion of the results, whilst some concluding remarks will follow in §7.

## 2 Observation and data reduction

The *ASCA* satellite (Tanaka, Inoue & Holt, 1994) observed NGC4051 during the AO2 phase between 6th July (15:28:34 UT) and 9th July 1994 (10:40:27 UT), for a total exposure time of  $\sim 1.55 \times 10^5 \text{ s}$ . The Solid State Imaging Spectrometers (SIS hereafter) were operating in 1 CCD mode and the data were collected in FAINT mode. Dark Frame Error (DFE) and echo corrections (Otani & Dotani 1994) were applied and the Charge Transfer Inefficiency (CTI) corrected Pulse Invariant SIS data used. Typical DFE values at the time when the observation was performed were  $\sim 1 \div 2 \text{ ADU}$ , corresponding to only  $\simeq 7 \text{ eV}$ , while the energy deficit for transfer was  $\sim 2 \div 3 \times 10^{-5}$  per transfer both for SIS0 and SIS1 chips used, which causes about 1% difference of the energy. Another source of gain uncertainties is the Residual Dark frame Distribution (RDD); for 1-CCD mode such effect is smaller than  $5 \text{ eV}$  even in the post-launch calibrations. The uncertainties on the energy scale that can be associated with such corrections can be therefore estimated as  $\leq 10 \text{ eV}$  in the lowest energy *ASCA* SIS band and  $\leq 20 \text{ eV}$  around  $6 \text{ keV}$ . A systematic error of such order has been taken into account in the forthcoming results. The Gas Imaging Spectrometers (GIS hereafter) were operating in PHA mode. Good time intervals for the data analysis have been selected according to the criteria in Table 1. They amount to a total integration time of  $\sim 6.8 \times 10^4 \text{ s}$  for both detectors. This

is more than twice the effective integration time of the PV phase observation. Photons were extracted from a circular area  $\simeq 4.7'$  of radius for the GIS and  $\simeq 3.2'$  for the SIS. Data preparation and selection were performed via the XSELECT package v.1.2; spectral fits were carried out using the XSPEC program, v.8.5 (Arnaud *et al.* 1991).

### 3 Temporal behaviour

Broadband light curves for the SIS0 and GIS2 detectors are displayed in Figure 1 (binning time  $\Delta t = 312$  s). Strong variability by a factor up to  $\sim 8$  on time scale  $\leq 10^4$  s is clear. Two flare-like structures can be recognized between  $10^4$  and  $3 \times 10^4$  s from the beginning of the observation and in the last  $10^4$  s. Events of very rapid variability with a doubling time of  $\sim$  few hundreds seconds are also relatively common.

X-ray variability on very short time scales has been reported by many authors. Doubling time scales of few  $\sim 10^3$  s were found by Marshall *et al.* (1983) with the Imaging Proportional Counter on board the *Einstein* satellite, by Lawrence *et al.* (1985) with the LE and ME *EXOSAT* detectors and by Matsuoka *et al.* (1990) in the 1987 *Ginga* observation. In Paper I, single episodes of flux doubling on time scales of the order of  $\sim$  few hundreds of seconds were reported. In order to characterize such variability from the statistical point of view, an analysis of the lowest-doubling times has been performed on the 100 s-binned light curves of all the four detectors. The results for the SIS0 and GIS2 are shown in Figure 2. The  $dN_{events}/d(\Delta t)$  distribution exhibits a flat behaviour with a sudden decrease below some typical time scale  $\tau$ . Fit of the distribution function of the form  $A[1 - e^{(-\Delta t/\tau)}]$ , where  $A$  is a normalization constant equal to the asymptotic mean of the distribution, yielded the values:  $\tau = 500 \pm 300$  s for SIS0 and  $\tau = 400 \pm 300$  s for GIS2 light curve, with a reduced  $\chi_r^2 \sim 1$ . We therefore conclude that NGC4051 presents broadband statistically significant variability on timescale as low as  $\sim$  few hundreds of seconds.

### 4 AO2 observation spectral analysis

Previous X-ray observations of NGC4051 showed a very complicated and variable spectral structure; in PV phase data a simple power law with photoelectric absorption by cold matter with cosmic abundance was too a simple model to explain the various features observed.

AO2 data confirm such outcomes in the light of a better S/N due to the more than doubled effective integration time. Background subtraction has been performed both with blank sky data files and with spectra obtained from a source-free region in the same FOV of the source. The results are fully consistent and the ones obtained with the former procedure are shown in the present paper. Spectral analysis has been restricted to the bands [0.57-10 keV] for the SIS and [0.7-10 keV] for the GIS detectors



in order to avoid low effective area energy channels and the systematic narrow-band spectral feature observed in the SIS spectra around the K neutral oxygen absorption edge ( $E \sim 0.54 \text{ keV}$ , Gendreau *et al.* 1995) that could significantly affect the results in the softer band. In Figure 3 the results of a fit with a simple photoelectric absorbed power law are shown. The  $N_H$  value has been constrained throughout the paper not to be lower than the Galactic value of  $1.3 \times 10^{20} \text{ cm}^{-2}$  (Dickey & Lockman 1990). The reduced  $\chi^2$  is rather poor in both cases ( $\chi^2_{SIS0+1} = 1644/601 \text{ d.o.f.}$ ,  $\chi^2_{GIS2+3} = 1633/1304 \text{ d.o.f.}$ ). The main contributions to the  $\chi^2$  are due to: a) a soft X-ray excess emission above the extrapolated power-law below  $E \sim 1 \text{ keV}$ ; b) a broad emission line feature centered at  $E \simeq 6.1 \text{ keV}$ .

The average source unabsorbed flux - calculated in the hypothesis of the phenomenological “L” model (see §3.1) - is  $2.6 \times 10^{-11} \text{ erg cm}^{-2} \text{ s}^{-1}$  in the 0.4–2.0 keV band and  $2.4 \times 10^{-11} \text{ erg cm}^{-2} \text{ s}^{-1}$  in the 2.0–10.0 keV band (average on the SIS spectra), corresponding to source-frame luminosities of  $0.58 \times 10^{42} \text{ erg s}^{-1}$  and  $0.54 \times 10^{42} \text{ erg s}^{-1}$  at  $z = 0.0023$ . Here and hereafter  $H_0 = 50 \text{ km s}^{-1} \text{ Mpc}^{-1}$  and  $q = 0.5$  are supposed. Such results are consistent with the 2–10 keV flux range observed by previous experiments ( $0.2 \div 5 \times 10^{-11} \text{ erg s}^{-1} \text{ cm}^{-2}$ ), including the PV *ASCA* observation ( $2.2 \times 10^{-11} \text{ erg s}^{-1} \text{ cm}^{-2}$ ).

## 4.1 Soft excess

In Paper I, Mihara *et al.* (1994) identified absorption edges features due to highly ionized oxygen species OVII and OVIII in the SIS NGC4051 spectra of PV phase data. The adding of such features to the simple absorbed power-law best-fit model, although statistically justified according to the F-test, is not able to remove the soft excess. A complete removal of the soft excess via narrow features (absorption edges and/or narrow emission lines with Gaussian dispersion  $\sigma$  fixed equal to 0) requires 6 lines in the energy range  $0.57 \leq E \leq 1.16 \text{ keV}$  and no edges with a  $\chi^2 = 661/594 \text{ d.o.f.}$  Such explanation, although statistically acceptable, is *de facto* simply a simulation of a continuum soft excess emission due to the limited energy resolution available; thus it will not be considered in the following.

Instead, adding a thermal continuum component (*i.e.* a blackbody) to the SIS spectrum produces a dramatic decrease of the  $\chi^2$  with  $\Delta\chi^2 = 876$ . However, even after this improvement narrow absorption features are clearly visible in the spectrum and can be modelled either with a couple of absorption edges and an emission line (hereafter Model L) or with three absorption edges (hereafter Model E), with comparable resulting  $\chi^2$  ( $\chi^2_L = 624.4/598 \text{ d.o.f.}$ ,  $\chi^2_E = 624.0/598 \text{ d.o.f.}$ ). The adding of each of the quoted features is justified according to the F-test as shown in Table 2, that contains the best-fit parameters for the models described. The fits in Table 2 have been performed on the spectral channels in the range [0.57–5 keV], in order to avoid contamination by the higher energy line structure. Here and hereafter errors are at 90% level of confidence for one interesting parameter ( $\Delta\chi^2 = 2.71$ , Lampton, Margon & Boyer 1976). This underestimates the actual 90% confidence region for multi-parameter fitting but nevertheless serves to provide an indication of the curvature of the  $\chi^2$  space near

the best-fitting points. Parameters with units of energies are quoted in the source reference frame. The energies of the softer two absorption edges ( $E_1 \simeq 0.74 \text{ keV}$  and  $E_2 \simeq 0.87 \text{ keV}$ ) are fully consistent – within the statistical uncertainties – with the K-shell photoionization energies of the oxygen ion species OVII and OVIII and will be therefore associated with them in the following. The depth of the OVII edge is almost the same in Model L and E ( $\tau \simeq 0.35$ ) while the OVIII depth is model-dependent, ranging from  $\tau^{(L)} \simeq 0.12$  to  $\tau^{(E)} \simeq 0.31$ . The narrow spectral features’ properties are not significantly dependent on the shape of the continuum, as shown in Table 2 where the best-fit parameters obtained when the blackbody is substituted by a bremsstrahlung, power-law, or multitemperature disk blackbody emission are shown. The temperature for optically thick emission is  $kT = 180 \pm 20 \text{ eV}$ . The best-fit blackbody parameters correspond to a typical emitting region size  $R_{bb} \sim 1.3 \times 10^{10} \text{ cm}$ , while the emission measure for optically thin thermal emission is  $n_e^2 V \sim 2 \times 10^{63} \text{ cm}$ .

It’s worthwhile to note that a standard scattering model (*i.e.* the superposition of power-law spectra with the same indices seen through different absorbing column densities) fails to reproduce the observed soft excess ( $\chi_r^2 \simeq 1.9$ , with significant residuals in the whole  $E \leq 2 \text{ keV}$  range).

If the average SIS spectrum absorption features are fit with only two absorption edges, as in Paper I, their energies turn to be  $E_1 = 0.738 \pm 0.013 \text{ keV}$  and  $E_2 = 0.927 \pm 0.017 \text{ keV}$ . This outcome is consistent with Paper I; however, according to the higher S/N AO2 data,  $E_2$  is more likely to be a blending of a double structured feature. If the model E (L) is applied to the PV phase data, the resulting optical depths are  $\tau_{OVII} = 0.26^{+0.20}_{-0.11}$  ( $\tau_{OVII} = 0.43^{+0.04}_{-0.03}$ ) and  $\tau_{OVIII} = 0.13 \pm 0.10$  ( $\tau_{OVIII} = 0.51 \pm 0.04$ ).

Some of these features lie within the useable energy bandpass of the GIS detectors. The soft excess in the GIS2 average spectrum can be modelled with a single absorption edge at  $E = 0.94 \pm 0.05 \text{ keV}$ , with  $\tau = 0.34 \pm 0.15$  and  $\Gamma = 1.88^{+0.04}_{-0.05}$  (F-test = 163); but fits with a comparable statistical significance can be achieved by the adding of an emission line at  $E = 0.81 \pm 0.03 \text{ keV}$  ( $EW = 70^{+20}_{-40} \text{ eV}$ ,  $\Gamma = 1.86^{+0.05}_{-0.06}$ ) for GIS2 and  $E = 0.80^{+0.03}_{-0.06} \text{ eV}$ , ( $EW = 60^{+20}_{-30} \text{ eV}$ ,  $\Gamma = 1.88^{+0.05}_{-0.06}$ ) for GIS3 or with a thermal continuum.

## 4.2 Warm absorber model

As already stated in §1, absorption features from highly ionized oxygen have been widely observed in the *ROSAT* and *ASCA* spectra of many Seyfert 1 galaxies and suggest the presence of warm matter along the line of sight. Models of absorption by ionized matter intervening along the line of sight (the so called “warm absorber”) can be calculated and compared with the available observational data, provided some simplifying assumption on the geometrical and physical properties of the absorbing matter are made. We have used the photoionization code CLOUDY (Ferland 1991) in order to calculate self-consistent total spectra resulting from the passage of ionizing continuum radiation through an optically- and geometrically-thin spherical shell. A power-law shape has been assumed for the incident spectrum in the whole energy range between 13.6 eV and 40 keV. A complete characterization of the physical properties of the absorbing matter is given once the parameter  $\xi \equiv L/n_e R^2$  is provided, where  $L$  is the luminosity of the ionizing continuum,  $n_e$  the numerical electron density and  $R$  the distance between the

central source and the inner edge of the shell. In fact the physical properties of the absorber matter depend on the ionizing flux  $F \propto L/R^2 = n_e \xi$ .  $n_e$  and  $\xi$  are supposed uniform inside the shell, while  $R = 10^{16}$  cm and  $L = 10^{43}$  erg s<sup>-1</sup>. The free parameters in such models are the photon index  $\Gamma$ , the ionization parameter  $\xi$  and the “warm” hydrogen column density  $N_W$ . A grid table model has been fitted to the SIS spectrum. Figure 4 shows the best-fit data/model ratio, with  $\chi^2 = 851/604$  d.o.f. The major contributions to the  $\chi^2$  are below  $E \sim 1$  keV, where the warm absorber features are present that should provide the bulk of information on the ionization state of the matter. The best-fit parameters are:  $\Gamma \sim 2.12$ ,  $\log(N_W) \sim 22.27$  and  $\xi \sim 110$ . A prominent emission-like feature is present at  $E \sim 0.90$  keV and the OVII edge looks not to be well modelled. An acceptable  $\chi^2$  can be obtained either through the adding of a thermal component, like a blackbody ( $\chi^2 = 694/602$  d.o.f.) or through the adding of three emission lines at energies  $E = 0.60 \pm 0.08$  keV,  $E = 0.69 \pm 0.08$  keV,  $E = 0.93 \pm 0.07$  keV ( $\chi^2 = 660/600$  d.o.f.), but in both cases the warm absorber matter best-fit parameters are not consistent with the presence of both OVII and OVIII ions [for example, in the latter:  $\log(N_H) \geq 22.50$ ,  $\xi = 162 \pm 12$ ]; such solutions, although statistically acceptable, have to be regarded only as purely mathematical. Thus the model does not provide a satisfactory explanation of the data as the approximations and assumptions appear to be too simple. A more detailed discussion on the properties of the absorbing matter implied will follow in §5, in the light of the variability properties that it displays.

### 4.3 Iron line emission

Adding a Gaussian emission line to the average spectra of both SIS and GIS detectors (in order to model the residuals around the Fe-K region) improves significantly the  $\chi^2$ . The best-fit parameters for a simple absorbed power-law and Gaussian line model are shown in Table 3, where only the channels with  $E > 2.3$  keV have been included in the fit in order to avoid contamination by the soft excess spectral components. The line centroid energy:  $E_{SIS} = 6.3 \pm 0.2$  keV and  $E_{GIS} = 6.0 \pm 0.3$  keV; the equivalent width is quite large compared to the typical values observed in Seyfert 1 galaxies ( $EW_{SIS} = 350_{-150}^{+170}$  eV) when compared to *Ginga* results. The line has a clear broad structure. Power-law photon index and normalization are  $\Gamma = 1.84_{-0.03}^{+0.05}$  and  $N_{pl} = 7.3_{-0.3}^{+0.5} \times 10^{-3}$  photons keV s<sup>-1</sup> cm<sup>-2</sup> at 1 keV respectively.

A detailed analysis of the emission feature reveals a much more complex structure.  $\chi^2$  is further improved by adding two narrow (*i.e.* Gaussian dispersion  $\sigma$  held fixed at 0) Gaussian emission components with energies  $E^{(2)} \simeq 6.4$  keV and  $E^{(3)} \simeq 5.5$  keV, albeit the significance of the third is somewhat marginal in the SIS spectra ( $\Delta\chi^2_{SIS} = 4$ ,  $\Delta\chi^2_{GIS} = 11$ ). The best-fit parameters for such fits are again summarized in Table 3. The presence of the new components affects slightly the centroid energy of the main component that decreases by  $\sim 2\%$ . We will refer to such multi-component structure as “emission complex” in the following.

Iron K-fluorescence line is considered as a typical signature of the reprocessing of the central source radiation by optically thick matter, possibly in the form of an accretion

disk around the putative black hole. Such a scenario, investigated by the works of Guilbert & Rees (1988) and Lightman & White (1988), predicts a continuum “bump” at energies  $E \geq 10 \text{ keV}$ . Since the appearance of the line and the excess continuum emission are thought to be strongly correlated, a power-law + reflection by a “cold” (*i.e.* not ionized) accretion disk + emission complex model has been applied both to the SIS and GIS data. The inclination of the disk has been fixed to  $\theta = 30^\circ$  (see below), but the dependency of the following results on this parameter is completely negligible. The only free parameter of the reflected spectrum is then the solid angle subtended by the reflecting matter  $\Omega/2\pi$ . Adding of this new degree of freedom is not justified according to the F-test ( $F_{GIS} = 1.0$ ,  $F_{SIS} = 0.1$ ); only a very loose constraint on the solid angle ( $\Omega/2\pi \leq 7$ ) is yielded if the model is applied on the spectra of the four detectors simultaneously. In the hypothesis of reflection by a plane-parallel slab ( $\Omega/2\pi$  held fixed to 1), the best-fit parameters for the main emission complex component are:  $E^{(1)} = 6.1 \pm 0.3 \text{ keV}$ ,  $\sigma^{(1)} = 0.7_{-0.5}^{+0.7} \text{ eV}$ ,  $EW^{(1)} = 220_{-150}^{+290} \text{ eV}$ , with an intrinsic photon index  $\Gamma = 1.88_{-0.04}^{+0.03}$ . The additional complex components have:  $E^{(2)} = 6.44 \pm 0.05 \text{ keV}$ ,  $EW^{(2)} = 60 \pm 30$ ,  $E^{(3)} = 5.50_{-0.19}^{+0.10} \text{ keV}$  and  $EW^{(3)} = 16_{-15}^{+26} \text{ eV}$  respectively. The contour plot for the centroid energy vs. the Gaussian dispersion of the main component is shown in the upper panel of Figure 5; at 90% level of confidence the Gaussian dispersion is  $\geq 0.2 \text{ keV}$ .

The total equivalent width of the emission complex is much higher than the average observed by *Ginga* in the same target ( $\langle EW \rangle_{NGC4051} = 140 \pm 70 \text{ eV}$ , Nandra & Pounds 1994), where a single “narrow” line was supposed. It is also much higher than the mean of the observed EW distribution in the complete *Ginga* Seyfert 1 sample ( $\langle EW \rangle_{Ginga} = 140 \pm 20 \text{ eV}$ , Nandra & Pounds 1994). However several Seyfert 1 observed by *ASCA* showed clearly a broad fluorescence iron line: IC4329A ( $\sigma_{99\%} \geq 0.15 \text{ keV}$ , Mushotzky *et al.* 1995, Cappi *et al.* 1996), NGC5548 ( $\sigma_{99\%} \geq 0.1 \text{ keV}$ , Mushotzky *et al.* 1995), MCG-6-30-15 ( $\sigma_{90\%} = 0.16_{-0.06}^{+0.10} \text{ keV}$ , Fabian *et al.* 1994). Complex and broad emission structures are to be expected if the emission originates in an accretion disk. As stated by many authors (Fabian *et al.* 1989, Matt, Perola & Piro 1991), the Doppler shifting, gravitational reddening and relativistic beaming are effective in altering the Gaussian profile of an emission line and producing a typical doubled-horned structure. Compelling evidence of such kind of structure in the *ASCA* observation of the Seyfert 1 MCG-6-30-15 (Tanaka *et al.* 1995) and of the intermediate Seyfert NGC4151 (Yaqoob *et al.* 1995) have been recently discovered, giving significant support for such a scenario.

In order to check quantitatively the disk hypothesis, line emission from a relativistic accretion disk model by Fabian *et al.* (1989) has been applied to the [2.3-10 keV] spectra of all detectors simultaneously. The free parameters are the inner ( $R_i$ ) and outer ( $R_o$ ) radii of the line emitting region in units of Schwarzschild radii  $R_S$  from the center and the inclination angle  $\theta$  between the normal to the plane of the disk and the line of sight. The energy of the line centroid  $E_\alpha$  has been held fixed to 6.4 (cold disk) and 6.7 (ionized disk). The emerging profile is also affected by the radial dependence of the emissivity, that in such a model is parameterized with a function  $R^{-q}$ . The underlying continuum is supposed to be a power-law with reflection by a plane-parallel slab and the disk-line inclination tied to the reflecting slab inclination. The best-fit parameters are listed in Table 4. The observed line is consistent either with a cold disk at moderate inclination ( $\theta \sim 30^\circ$ ) or with an almost face-on ionized disk.  $R_i$  is  $\sim 10R_S$ , while only in the cold disk case  $R_o$  can be constrained to a value  $\sim 30R_S$ . In the cold case the derived EW is

higher than the maximum allowed by presently available models with solar abundance, by a factor  $\sim 1.5$ .

We stress that no absorption edge by neutral or ionized iron has been detected in the average AO2 SIS spectra. Upper limits on the optical depth for some trial energies have been:  $\tau_{FeI}(E = 7.11 keV) < 0.06$ ,  $\tau_{FeXX}(E = 8 keV) < 0.19$ ,  $\tau_{FeXXIV}(E = 8.80 keV) < 0.05$ .

## 5 Spectral variability

NGC4051 is known to be a variable X-ray source. Both *EXOSAT* (Lawrence *et al.* 1985) and *Ginga* (Matsuoka *et al.* 1990) observations showed a hardening of the spectrum for decreasing flux; in both cases it was described in terms of decrease of the spectral photon index. On the other hand, Kunieda *et al.* (1992) analyzed successfully the spectrum of the May 1988 *Ginga* observation in terms of reprocessing of the nuclear radiation by blobs of matter ( $N_{blob} \sim 10^{24.5} cm^{-2}$ ). Significant spectral changes accompanied flux variations by a factor of 2–3 within 1000 s in the softer *Ginga* band (2.3–6.4 keV), but they did not strictly follow the luminosity trend; instead, it was possible to distinguish three different phases, characterized by a constant hard (*i.e.* 8.7–20.9 keV) flux with hard spectrum, by a low energy flare with soft spectrum and by a soft spectrum with almost synchronized flux variability respectively. Such complex spectral changes could be successfully explained by changes of the intrinsic luminosity and the blob number along the line of sight. Fiore *et al.* (1992a) re-analyzed all the *Ginga* NGC4051 observations in the framework of two-component models (power-law + reprocessing) and affirmed a simultaneous variation of both. A 99% level of confidence variability of the iron line correlated with that of the underlying continuum down to time scales as short as few thousands seconds gave further support to such hypothesis.

The *ASCA* AO2 observation data provide a lot of information about the variability of the source and allow to deliver new insight on this topic. In the following the soft excess and intrinsic power-law photon index variability will be mainly addressed, both via hardness ratio analysis and via direct comparison of spectral fits performed on different intensity phases.

### 5.1 Hardness ratio analysis

The broadband spectrum of the NGC4051 AO2 *ASCA* observation shows flux-dependent changes at both low and high energies. The PHA ratio of the average SIS0 spectra corresponding to a High and Low intensity State is shown in Figure 6. An operative definition of the procedure followed to select High and Low State photons will be given in §5.2. The High State spectrum is harder for  $E \geq 2 keV$  and  $E \leq 1 keV$ .

A useful tool for characterizing the spectral variability of X-ray sources is the study of Softness Ratio (*SR* hereafter). The energy bands have been chosen in such a way they are representative of the behaviour of different spectral components; according to Netzer, Turner & George (1994) the most suitable choice is the bands: [0.7–1.3 keV] and

[2.5-5 keV]. The  $SR$  is therefore defined as:

$$SR = \frac{CR [0.7-1.3 \text{ keV}]}{CR [2.5-5.0 \text{ keV}]} \quad (1)$$

Such choice allows to study the differential variability of the spectral components. Warm absorber should predominantly affect the flux in the softer band. The low energy cut-off of the harder band has been chosen in order to avoid contamination by the iron line emission complex.

In Figure 7 the SIS0+1 light curve in the two bands and the  $SR$  light curve are shown for a binning time  $\Delta t = 500 \text{ s}$ . The  $\chi^2$  for constant hypothesis of the  $SR$  light curve is  $\chi^2_{SR} = 341.2/61 \text{ d.o.f.}$  The  $SR$  undergoes a significant variability, getting lower for increasing flux and higher for decreasing flux. When the source flux approaches its minimum throughout the observation ( $1.2 \times 10^5 \text{ s}$  after the start), the  $SR$  doubles within a time scale  $\sim 10^4 \text{ s}$ . A decrease of comparable order of magnitude seems to be associated with the sudden doubling of flux within  $\sim$  few thousands of second after  $\sim 10^4 \text{ s}$  from the start.

The determination of the correct variability timescale is of the utmost importance in order to derive meaningful constraints on the geometry and physical processes involved in Active Galactic Nuclei (AGN hereafter). The  $SR$  dependency on the total count rate has then been studied in detail. In Figure 8 the  $SR$  is plotted vs. the total [0.7-5 keV] count rate (binning time  $\Delta t = 5000$ ). The  $\chi^2$  for constant hypothesis is  $\chi^2 = 259/29 \text{ d.o.f.}$ , corresponding to a chance occurrence likelihood  $P < 0.1\%$ . Also the linear correlation coefficient is rather high ( $r_{29} = 0.73 \pm 0.05$ ), again corresponding to a chance occurrence likelihood  $< 0.1\%$ . A careful visual inspection at the  $SR$  light curve in Figure 7 would suggest the highest variability to be concentrated in the  $\sim 2 \times 10^4 \text{ s}$  time interval when the source flux is minimum. The same analysis as above has then been repeated excluding it from the light curves; however the strong  $SR$  vs.  $CR$  correlation has been confirmed ( $\chi^2 = 131/24 \text{ d.o.f.}$ ,  $r_{24} = 0.64 \pm 0.10$ ,  $P < 0.1\%$  for both parameters). Similar results are obtained for binning times  $\Delta t = 500 \text{ s}$  ( $\chi^2 = 320/61 \text{ d.o.f.}$ ,  $r = 0.73 \pm 0.05$ ) and  $\Delta t = 25000 \text{ s}$  ( $\chi^2 = 151/6 \text{ d.o.f.}$ ,  $r = 0.95 \pm 0.03$ ,  $P \simeq 0.5\%$ ). The binning time is obviously limited by the total elapsed time of the observation ( $T_{elaps} \sim 1.5 \times 10^5 \text{ s}$ ), and no significant piece of information can be derived for  $\Delta t > 25000 \text{ s}$ . Anyway, there is compelling evidence of an increase of the  $SR$  when the source flux increases on the whole two order of magnitude range between  $\Delta t \sim 10^2 \text{ s}$  and  $\Delta t \sim 10^4 \text{ s}$ . That evidence can naturally be explained in terms of a lower hard flux or weaker absorption by ionized matter when the source is more intense or any combination of the two. In order to disentangle the two effects (or others that might be present) a detailed time-resolved analysis of the various spectral components is needed.

## 5.2 Spectral analysis: soft excess

The high effective integration time allows a detailed time-resolved analysis of the main grand spectral features discovered in the NGC4051 average spectrum. For such purpose, the whole observation has been divided into 11 contiguous segments according to the following procedure: a  $\Delta t = 100 \text{ s}$  light curve has been extracted and all the consecutive

bins whose count rate was higher than the total mean count rate have been gathered together (contamination not higher than  $\sim 12\%$  has been allowed). The same procedure has been followed for bins whose count rate was lower than the total mean count rate. The log of the resulting subdivisions is shown in Table 5. Each of such subdivision will be referred to as *orbit* in the following, although they have no relation with the real orbits of the *ASCA* satellite. The span of each orbit is never less than  $\sim 7 \times 10^3$  s except in the case of the 3rd orbit whose time span is  $\sim 4 \times 10^3$  s. The count rate for each orbit is in the range 60% – 144% of the total mean count rate. The minimum flux episode is included in the 10th orbit, the flare-like structures in the 2nd and 11st.

The best-fit optical depths for OVII and OVIII edges when Model L is applied to the combined SIS0+1 spectrum of each orbit are shown in 5th and 6th columns of Table 5. In such fits the energies of the edges are frozen to their best-fit values in the average spectral fit due to low S/N. The 10th orbit OVII optical depth is significantly higher than the mean. For the sake of a deeper investigation, we have gathered together the orbits 1+3+5+7+9+11 (hereafter referred to as High State, HS) and the orbits 2+4+6+8+10 (Low State, LS) and applied Model E and L to the SIS HS and LS spectra. The results are summarized in Table 6. The OVII optical depth undergoes a significant (90% level of confidence) change by a factor  $\sim 50\%$ , the edge energies remaining consistent within the quoted statistical uncertainties. No significant variation is observed either for energy or optical depth of the OVIII edge. A further detailed analysis has been performed splitting the 10th orbit from the rest of Low State, in order to check the significance of the outcomes summarized in Table 5. We will refer hereafter to the Low State phase when the 10th orbit is subtracted as LS\*. A 99% level of confidence contour plot for the OVII edge energy vs. optical depth when the L model is applied to HS, LS\* and 10th orbit is plotted in Figure 9. The 10th orbit and HS optical depths are different at more than 99% level of confidence, whilst the LS\* optical depth is not consistent with the other two phases' at only 90% level of confidence. At this latter level, however, it can be stated that a smooth trend of decreasing of OVII optical depth with increasing flux is observed on timescales as low as  $10^4$  s, and then its variability is not limited at the lowest flux interval. No significant variability within the quoted statistical uncertainties is instead detected for the OVIII absorption edge (see Figure 10).

The spectral shape in the lowest energy *ASCA* band is very complex; the observed variability of the narrow-band features might be due to the interplay between the ionized absorption and the continuum soft excess component. It must be remembered however that the “L” model comprises self-consistently all the spectral components required to remove the soft excess. Moreover, the observed variability patterns are almost independent of the detailed shape of the soft continuum component used. In Figure 11 the optical depth vs. energy contour plots are shown when a bremsstrahlung or power-law models replace the blackbody. Analogous conclusions can be derived about the edges' variability. The continuum models in Figure 11 are likely to be less physically meaningful explanations of the observed soft excess emission; but the lack of any significant dependency of the narrow-band feature results on the underlying continuum spectral shape gives strong support to their reality.

### 5.3 Spectral analysis: power-law photon index

The 7th row of Table 5 shows the best-fit value that the power-law photon index  $\Gamma$  assumes when the L model is applied. It is significantly variable ( $\chi^2$  for constant hypothesis 28/10 d.o.f.) and appears to be correlated with the total flux ( $r_{10} = 0.8 \pm 0.3$ ). If the soft excess is efficiently removed by models “E” or “L”, this should be an indication of a real variation of the observed underlying continuum photon index.

Assessing unambiguously an intrinsic variation of the spectral index is however a very difficult task if the *ASCA* data alone are available. Any variation in the relative normalization of the direct and reflected components might produce an apparent change in the steepness of the spectrum. If, as the outcomes in §4.3 might suggest, the iron line comes from a relativistic accretion disk, its broad and skewed structure might give a significant contribution to the photon emission in the 4-8 keV range. Last, but not least, absorption by ionized matter might affect the high energy spectrum also above 2.3 keV. The limited *ASCA* high energy bandwidth does not give a good statistics above  $\sim 8$  keV and it is thus difficult to constrain the spectral shape in the hard tail. Having all such problems in mind, we searched for index changes, provided a self-consistent physical model with some simplifying assumptions is assumed, in order to reduce the number of degrees of freedom; namely:

- i) we assumed a power law spectrum + reflection by a plane-parallel infinite slab + iron emission line complex.
- ii) The fainter components’ parameters have been held fixed to their average best-fit value (see §4.3)
- iii) neither the absorbing medium nor the continuum soft excess component have been supposed to affect substantially the spectral shape for  $E \geq 2$  keV. That implies the numerical density of the intervening matter  $\leq 10^{22} \text{ cm}^{-3}$  and the temperature of the blackbody of the order at most few hundreds eV. Both conditions are fulfilled in the *ASCA* data according to the low energy bandpass outcomes (see §6.2)

Such a model has been fitted to the SIS+GIS spectra obtained when the following orbits are gathered together: 8+10 (1st quartile), 2+6 (2nd quartile), 4+5+7+9 (3rd quartile), 1+3+11 (4th quartile). The relative normalization between the direct and reflected components has been kept constant ( $\Omega/2\pi = 1$ ) or allowed to vary inversely to the flux; such two cases simulate an immediate or delayed response of the reprocessing to nuclear flux changes respectively. In the latter scenario, the intrinsic width of the main emission complex component has been held fixed to its average best-fit value in order to further reduce the available degrees of freedom. The best-fit parameters are listed in Table 7 and 8.  $\Gamma$  shows the same qualitative trend in both cases. In Figure 12 a plot of the  $\Gamma_{2.3-10\text{keV}}$  vs. the [2-10 keV] luminosity is shown in the constant normalization ratio case. The figure includes also two measures when the same model is applied to the spectra of the HS and LS PV phase data (the definition of the intensity phase in PV data is analogous to the AO2 case). If all the six experimental points are taken into account the index is variable ( $\chi^2$  for constant hypothesis 33/5 d.o.f.) and correlated with the



[2–10 keV] luminosity ( $r_6 = 0.88 \pm 0.08$ , the lower limit corresponding to a likelihood of casual occurrence  $P < 6\%$ ). Such correlation is valid also if only the four experimental points relative to the AO2 data are considered ( $\chi^2$  for constant hypothesis 31/3 d.o.f.,  $r_4 = 0.98 \pm 0.04$ ,  $P < 25\%$ ). In Figure 12 it is straightforward to see that the PV phase measurements are not aligned exactly with the same straight line corresponding to the AO2 measures. A secular pattern of variability could therefore be superimposed on the short timescale correlation between spectral index and luminosity. If the PV phase experimental points are arbitrarily shifted rightward by an amount  $\sim 20\%$ , the alignment is qualitatively much better and the linear correlation coefficient  $\Gamma$  vs.  $L$  turns to be consistent with 1 even for all the six measures ( $r_6 = 0.97 \pm 0.04$ ); we remind here that the average [2–10 keV] flux of the AO2 observation is just 20% higher than the flux of the PV phase data in the same energy range. Hysteresis phenomena in the  $\Gamma$  vs.  $L$  relation should be expected if the continuum is produced in a pair dominated Comptonized non-thermal plasma (Yaqoob 1992). If we take the extreme points in Figure 12 as representative of the low and high state of the source, the pivot point for spectral change is  $E_p \simeq 20$  keV.

Next question to be addressed is whether the observed changes in the spectral index are really due to changes in the slope of the intrinsic power-law. As stated in section 4.3, the presence of the iron line is supposed to be correlated to a “bump” of continuum emission at energies  $E \geq 10$  keV. Differences in the observed photon index could therefore be due to different amount of reflected flux, with the stronger reflection producing a flatter spectrum. In order to check this hypothesis we have first calculated the ratio between the photon indices in the [2.3–5.0 keV] and [5.0–10.0 keV], the former band likely to be unaffected by any reprocessed component; the measure of such ratio for all the quartiles is reported in 6th column of Table 7. Although a slight trend of decreasing of such ratio with increasing luminosity can be noticed, all the values are consistent with 1. As a further check, fits have been performed when the  $\Omega/2\pi$  parameter in the reflection model is left free. The adding of this further degree of freedom is not statistically justified for any of the AO2 quartiles (see 7th column in Table 7) and in neither the HS nor the LS phase in PV data.

We conclude therefore that the  $\Delta\Gamma \sim 0.4$  variation observed in the *ASCA* data of NGC4051 might be interpreted as due to an intrinsic index change in the framework of a self-consistent physical model that takes into account all the spectral components in the reflecting accretion disk scenario. Such outcomes partly confirms the results of Matsuoka *et al.* (1990).

## 6 Discussion

### 6.1 Broadband variability

The outcomes presented contribute to shed new light on the spectral properties of the X-ray emission from AGNs and allow to set constraints on the geometrical and physical properties of the processes involved.

The main source for the huge amount of power emitted by the nuclear region of AGN is the conversion of gravitational to radiative energy in matter falling onto a

supermassive central accretor. NGC4051 is well known as one of the most variable extragalactic sources; *ASCA* observations revealed flux changes by a factor of 8 within typical timescale  $\sim 10^4$  s and doubling time  $\sim$  few hundreds seconds. The *ROSAT* light curve in the softer [0.1–2.4 keV] range displayed variations by a factor  $\sim 10$  within  $\sim 4 \times 10^4$  s (McHardy *al.* 1995). Light crossing time arguments yield an upper limit for the mass of the central object  $M \leq 10^7 M_\odot$  if the size of the emission region is as large as 5 Schwarzschild radii. We stress that previous estimates based on the correlation between the iron line emission strength and the underlying continuum intensity - that yielded values by a factor of 5 lower - are not confirmed by the *ASCA* data, since no flux-correlated variability of the iron line could be firmly assessed within the 2 days AO2 observations (cfr. Table 7). The required efficiency in converting accreting matter to luminosity (Fabian & Rees 1979) is  $\geq 10^{-3}$ , consistent with accretion onto a Schwarzschild black hole.

## 6.2 Identification of the third narrow low-energy spectral feature

The AO2 spectra have provided further confirmations of the presence of narrow features due to absorption by highly ionized matter. Better AO2 data S/N ratio has allowed to recognize the absorption edge discovered in PV phase data at energy  $E \sim 0.92$  keV as probably due to blending of two different features. Two edges at energies  $E \sim 0.74$  keV and  $E \sim 0.86$  keV have then been detected in the AO2 SIS spectrum, whose energies are fully consistent with the K-photoionization energies of the ionized oxygen species OVII and OVIII. A third narrow feature is statistically required to model the spectrum, but it is not possible to distinguish between a further absorption edge or an emission line from a purely statistical point of view. A correct identification of the nature of this third feature is of primary importance, also because the OVIII absorption edge optical depth is strongly model dependent. We will therefore address this topic in this section.

Provided this third feature is an absorption edge, it could be a blending of the K-photoionization edges of NeIII and/or NeIV ( $937 \leq E \leq 971$  eV) or a blending of L-photoionization edges of FeVII÷X ( $930 \leq E \leq 1000$  eV). If such species are to be located in the same physical region as OVII and OVIII, the ionization structure and temperature of the corresponding absorbing matter has to be the same. In the “E” model the typical values of oxygen optical depths are  $\tau_{OVII} \sim 0.35$  and  $\tau_{OVIII} \sim 0.12$ , corresponding to hydrogen equivalent column density of  $N_H(OVII) \sim 1.6 \times 10^{21} \text{ cm}^{-2}$  and  $N_H(OVIII) \sim 1.3 \times 10^{21} \text{ cm}^{-2}$ . The range of ionization parameters that allows an abundance ratio  $[OVII]/[OVIII] \sim 1$  for a cloud of gas in photoionization equilibrium is relatively narrow ( $\xi = 50 \div 90 \text{ erg cm s}^{-1}$ , Kallmann & McCray 1982), with typical plasma temperature  $\sim 2 \times 10^5$  K. On the other hand, the presence of NeIII/NeIV or FeVII÷X species implies  $\xi$  not to be higher than 25. Moreover the equivalent hydrogen FeVII÷X column density required would be  $\sim 8 \times 10^{22} \text{ cm}^{-2}$ . One could suppose the oxygen features to be produced in a physically different region than the third absorption feature; such complication looks however unnecessary, although it cannot be ruled out *a priori*.

A plasma in photoionization equilibrium with an ionizing continuum is expected to emit a rich spectrum of X-ray lines as the result of collisional excitation, inner shell fluorescence and recombination. Line-like features with typical  $EW \sim 30 - 100$  eV were

detected in the *Einstein SSS* spectra of several Seyfert 1 galaxies (Turner *et al.* 1991) and suggested to originate in a hot ( $T \sim 10^7$  K) collisionally excited plasma. However subsequently Netzer (1993) pointed out that photoionized gas might be responsible for them. One of the most promising candidates in the range of the observed NGC4051 line(s) ( $\lambda$  13.0 – 13.5 Å) is L-shell iron line-complex which can cover the whole range between 0.7 and 1.6 keV (Band *et al.* 1990, Liedhal *et al.* 1990). However, iron L-shell lines should dominate the spectrum for values of the ionization parameters  $U \equiv F_{ion}/N_H c > 10$ , where  $F_{ion}$  is the ionizing continuum flux and  $c$  is the speed of light. That corresponds to  $\xi \geq 100$ , slightly higher than the one inferred by the oxygen ions abundance. Line-like features with energy  $\sim 900$  eV could therefore be likely produced by OVII and OVIII continua or NeVII/IX  $L_\alpha$  lines.

### 6.3 Warm absorber variability

The presence of absorption edges due to highly ionized oxygen advocates for a distribution of matter along the line of sight whose ionization structure is – partly or totally – sustained by the radiation emitted by the AGN central source. In such physical conditions, the state of the matter can be parametrized through the electronic temperature  $T$  and an ionization parameter like  $\xi$  or  $U$ . Krolik, McKee & Tarter (1981) showed that in conditions of thermal and ionization equilibrium matter should be thermally stable only in two phases: a cold ( $T \leq 10^5$  K) phase with lower ionization states and a hot ( $T \geq 10^7$  K) phase with higher ionization states. However, a recent paper by Reynolds & Fabian (1994), stated the existence of a possible intermediate stable state with typical  $T \sim 10^5$  K and  $\xi \sim 10^{1.5-2}$ , which they proposed to be a good candidate for the warm absorber. Such state would be consistent with the co-existence of OVII and OVIII species; the range of allowed ionization parameters is relatively narrow [ $\Delta\Xi/\Xi \sim 0.1$ , where  $\Xi \equiv (2 \times 10^4 \text{ K}/T)\xi$ ] and that allows to study the warm absorber variability in terms of fluctuations around a stable state where both OVI and OIX numerical density is negligible if compared to the prevailing oxygen ions.

The detected variability of absorption features in the *ASCA* AO2 observation of NGC4051 allows to put some constraints on the geometrical and physical properties of the absorbing matter. At first we suppose density and ionization parameter of the absorbing matter to be uniform (one-zone hypothesis) and the ionization structure to be driven predominantly by the photoionization equilibrium. In such hypothesis the relevant time scales for each ionized species are the radiative recombination and the photoionization time scale to be compared with the typical variability time scale  $t_{var} \sim 10^4$  s. The most natural explanation for the decrease in the OVII edge optical depth with increasing flux is the increasing in the amount of photoionization processes OVII→OVIII. The typical ionization timescale can be expressed as (*e.g.* Otani 1996):

$$t_{ph}^{OVII} \sim 80 \left( \frac{100}{\xi} \right) \left( \frac{10^9 \text{ cm}^{-3}}{n_{OVII}} \right) \left( \frac{E_{edge}}{1 \text{ keV}} \right) \left( \frac{10^{-19} \text{ cm}^{-2}}{\sigma_{ph}(E_{edge})} \right) s \quad (2)$$

$$\simeq 4 \times 10^{10} / n_{OVII} \text{ s}$$

where  $n_{OVII}$  is the numerical hydrogen equivalent density of OVII and  $\sigma_{ph}(E_{edge})$  is the photoionization cross-section at the absorption edge energy. From the condition  $10^4 \text{ s} \geq t_{var} \geq t_{ph}$  it is possible to set  $n_{OVII} \geq 4 \times 10^6 \text{ cm}^{-3}$ , that implies a lower limit

for the density of the absorbing matter  $n \geq 2.1 \times 10^{10} \text{ cm}^{-3}$  assuming cosmic oxygen abundances.  $t_{ph}$  can be also expressed as a function of physical parameters of the warm absorber:

$$t_{ph}^{OVII} \sim 20 R_{16}^2 L_{43}^{-1} \text{ s} \quad (3)$$

where  $R_{16}$  is the distance of the warm absorber from the nuclear source in units of  $10^{16} \text{ cm}$  and  $L_{43}$  the X-ray luminosity in units of  $10^{43} \text{ erg s}^{-1}$ . The variability constraint implies therefore  $R_{16} \leq 7$ . If the change of the photoionization opacity produces a change in the column density  $\Delta N_H \sim \Delta R n$ , it follows  $\Delta R \leq 3 \times 10^{15} \text{ cm} \ll R$ . That should be suggestive either of geometrically thin or – more likely – of a quite small filling factor for the distribution of the absorbing matter.

A change in the column density of the absorbing OVII should be accompanied by an opposite change in the OVIII column density. However, in the *ASCA* NGC4051 data there is no clear evidence of such change. The relevant time scales involved for the OVIII balance are the recombination timescale  $t_{rec}$  for the OVIII→OVII process and the photoionization timescale  $t_{ph}^{OVIII}$ . The former is expressed by (*e.g.* Otani 1996):

$$t_{rec} \sim \frac{1}{\alpha_{rec} n_{OVIII}} \quad (4)$$

$$\simeq 2 \times 10^7 \frac{T^{0.76}}{n_{OVIII}} \sim 2 \times 10^{11} / n_{OVIII} \text{ s}$$

In the framework of the “L” model,  $n_{OVIII} \sim 3n_{OVII}$  and  $t_{rec} \sim t_{ph}^{OVII}$ . The condition of ionization equilibrium for OVII is therefore likely to be fulfilled. In the meanwhile, the OVIII photoionization timescale is given by:

$$t_{ph}^{OVIII} \sim 1.3 \times 10^{11} / n_{OVIII} \text{ s} \quad (5)$$

according to equation 2. Then  $t_{rec} \sim t_{ph}^{OVIII}$  and that could contribute to keep the OVIII species constant.

Similar evidence of such uncorrelated variation of ionized oxygen edges has been observed in the *ASCA* observation of MGC-6-30-15 (Reynolds *et al.* 1995, Otani *et al.* 1996), where a significant change in the absorption optical depth of OVIII was detected with no appreciable change in OVII. A stratification of the absorbing medium was claimed as a possible interpretation. A recent paper by Krolik & Kriss (1995) has pointed out that there is no reason *a priori* for imposing either the thermal equilibrium or the ionization balance; whether or not they are fulfilled depends strongly on the detailed ionization structure, on the mean luminosity and variability features of each AGN. The presence of resonance scattering lines can moreover greatly affect both the energy and the optical depth of the observed absorption features, leading to an incorrect interpretation of absorbing medium properties. Taking that into account can lead, for instance, to a dramatically different interpretation of the low-energy spectral variability in MGC-6-30-15, suggesting a fixed column density and ionization equilibrium scenario. Some caution must then be employed in the interpretation of the NGC4051 quoted results and only high resolution spectroscopy in the soft X-ray band will be able to solve all the puzzling questions still open.

## 6.4 Photon index variability

*ASCA* detected a significant ( $\Delta\Gamma \sim 0.4$ ) and robust change of the photon index for a factor of 4 flux variation. A still higher variability ( $\Delta\Gamma \sim 0.7$ ) had been found in *Ginga* data (Matsuoka *et al.* 1989), although a possible explanation in terms of variable absorption could account for the data equally well (Fiore *et al.* 1992b). The broadband *ASCA* coverage and the improved high energy resolution have allowed to conclude that at least part of such variability can be explained in terms of intrinsic photon index variation.

An analogous change in the power-law slope was found by Leighly *et al.* (1996) in the *ASCA* observation of the Narrow Line Seyfert Galaxy Mrk766, that showed a  $\Delta\Gamma = 0.4$  for a flux variation by a factor of  $\sim 2$  on typical timescales  $\sim$  few thousands of seconds. A renewed interest has thus recently arisen about such topic.

The most successful model for the continuum production in AGN is the Comptonization of UV or soft X-ray seed photons, which probably originate in an accretion disk, by a distribution of relativistic electrons. Depending on the nature of the injected electron distribution such models can be *thermal* or *nonthermal*. A spherical geometry for the interaction region is assumed with radius  $R$  and luminosity  $L$ , but a fairly independent description by the details of the involved geometry can be achieved if the dimensionless luminosity to size ratio, or *compactness parameter*  $\ell$  is introduced (Cavaliere & Morrison 1980, Guilbert, Fabian & Rees 1983), defined as:  $\ell \equiv \frac{L}{R} \frac{\sigma_T}{m_e c^3}$ , where  $\sigma_T$  is the Thompson scattering cross section. A further ingredient in such models is the  $\gamma$ -ray absorption via electron-positron pair production; the optical depth of such a process is  $\geq 1$  for  $\ell \geq 10$  (Svensson 1994). Provided the constraint on  $R$  from the lowest doubling time scale  $R < 1.5 \times 10^{13}$  cm holds and the observed 2-10 keV luminosity  $\sim 10^{42}$  erg s $^{-1}$ ,  $\ell_X \geq 2$  and  $\ell_e$  of the injected electron distribution can be higher by an order of magnitude if NGC4051 reproduces the multifrequency spectral behavior of NGC4151 (Yaqoob 1990). The condition for pair reprocessing could then also be achieved in NGC4051.

The relation between power-law spectral photon index and physical parameters in the simple case of an unsaturated thermal Comptonized model has been derived analytically by Rybicki & Lightman (1979).  $\Gamma$  depends inversely on the Compton parameter  $y \equiv \frac{4kT}{m_e c^2} \tau_{es}^2$ . We could therefore suppose the change in the observed [2–10 keV] spectral index to be due to the gradual increase of  $kT$  with decreasing flux. However, if the soft photon input is constant, the pivot point should yield an estimate of the energy of the soft photons distribution, which is not compatible with the observed value of  $E_P \simeq 20$  keV (see §5.3). Moreover, recent calculations by Chakrabarti & Titarchuk (1995) have shown that spectral photon index as low as 1.5 can be only achieved for a small part of the parameter space with a thermal distribution of nonrelativistic electrons and  $\Delta\Gamma = 0.5$  requires variations of the accretion rate of two order or magnitude. Such kind of dramatic flux changes has never been detected in NGC4051, although they are not rare in Narrow Line Seyfert Galaxies.

A recent paper by Ghisellini & Haardt (1994) demonstrated that it is possible to set a one-to-one correspondence between  $\Gamma$ ,  $T$ ,  $\ell_e$  and  $\ell_s$ , provided that the thermal plasma is pair-dominated. The *starvation ratio*  $\ell_e/\ell_s$  is fixed once the photon index is known and the  $\ell_e$  spans more than 3 order of magnitude with the variation of the temperature of plasma in pair equilibrium. Numerical simulations shows that  $\Delta\Gamma \sim 0.4$  requires a variation of the starvation ratio  $\sim 40$ ; that implies at least a factor of 10 of

variation for the soft-energy seed photon intensity. These numbers are in fairly good agreement with the observed *ROSAT* variability (McHardy *et al.* 1995); the upper limit on the central black hole mass is two order of magnitude higher than that derived from the broadband *ASCA* variability (see § 6.1) if the *ROSAT* time scale corresponds to the dynamical time scale of the innermost allowed Schwarzschild orbit. However the maximum dynamical range of the soft excess continuum component allowed by *ASCA* data is only  $\sim 2$  ( $1.0 \times 10^{-11} \leq F_{bb} \leq 2.0 \times 10^{-11} \text{ erg s}^{-1} \text{ cm}^{-2}$  if the “L” model is applied to the spectra of the quartiles phases). Therefore no evidence of the required dramatic flux variability of the soft input component arises from the *ASCA* data; that casts some doubt on the validity of such scenario for NGC4051.

An alternative explanation is provided by the non thermal Comptonization models. With the most simplifying assumptions, soft photons with a blackbody distribution peaked at energy  $x_s \equiv 2.8kT/m_e c^2$  interact with a monoenergetic distribution of relativistic electrons with Lorentz factor  $\gamma_0$ . The compactness parameters  $\ell_e$  and  $\ell_s$  are defined as above. A steady distribution of primary particles produces a spectral photon index  $\Gamma \sim 1.5$ ; if every scattered photon makes a pair with equidistributed energies, the emerging spectrum of the second generation will have  $\Gamma \sim 1.75$ . If pair saturation is achieved through successive pair cascades, the value of the slope tends to  $\Gamma \sim 2$ , which is consistent with the observed results and could explain the “saturation” effect shown by the  $\Gamma_{2-10 \text{ keV}}$  vs.  $L$  relation in the present analysis. Yaqoob (1992) studied in detail the physical condition for the photon index variability observed in the Seyfert 1.5 galaxy NGC4151 to be achieved. The observed index–flux correlation in NGC4051 can be reproduced by a variable Lorentz factor and a constant electron injection rate, with correlated input UV variations in order to leave  $\ell_s/\ell_e$  constant. If the Lorentz factor varies by a factor of  $\sim 2$  it is constrained to lie between  $\sim 80 \left( \frac{3 \times 10^{-5}}{x_s} \right)^{1/2}$  and  $\sim 1100 \left( \frac{3 \times 10^{-5}}{x_s} \right)^{3/4}$ .

Similar conclusions were derived in a recent paper by Torricelli-Ciamponi & Courvoisier (1995), but in a slightly different scenario. In their numerical model, both the thermal UV emission and the inverse Compton reprocessing take place in the same hot plasma cloud. It need not to be small in size nor optically thick to pair production and the UV reprocessed photon luminosity is only a fraction of the observed. If the observed X-ray continuum soft component is the hard tail of an observed UV, there is therefore no need for any correlated variability with the high energy (*i.e.* 2-10 keV) flux. The authors applied their numerical model to the  $F_{2-10 \text{ keV}}$  vs.  $\Gamma$  relation in Matsuoka *et al.* (1990) and derived a characteristic size of the cloud  $\sim 10^{14} \text{ cm}$  and a UV spectrum  $kT \sim 30 \text{ eV}$ . Comparable results might be expected if the fit were to include also the outlined *ASCA* results. But the idea that the thermal and non-thermal radiation to be emitted in the same physical region is not strongly supported by the current analysis, regardless of the optical properties of the emitting plasma. If we suppose an optically thin cloud with a numerical density from the Torricelli-Ciamponi & Courvoisier model ( $n \sim 7 \times 10^{10} \text{ cm}^{-3}$ ), its typical size is  $\sim 5 \times 10^{13} \text{ cm}$ ; that implies  $M_{bh} \sim 10^8 M_\odot$ , which is one order of magnitude higher than the upper limit imposed by the X-ray variability pattern (see §6.1). On the other hand, a slight trend of correlated increase of the thermal emission with flux on timescales as low as several  $10^4 \text{ s}$  might suggest to locate an optically thick emitting region at  $\sim 10^3 R_s$ . In such a case, the characteristic temperature  $T \simeq 180 \text{ eV}$  is somewhat higher than expected from the innermost region of an optically

thick disk, but it is fully consistent with the temperature required in a warm absorbed power law + blackbody fit of a combined *ROSAT* and *Ginga* spectrum (Pounds *et al.* 1994). Such outcome might be connected with the low luminosity and black hole mass, although it cannot rule out the effect of Comptonization on the inner disk emission. Moreover it must be taken into account that the *ASCA* low energy limited bandwidth alone is not the most suitable for the exact determination of the temperature of any UV-soft X-ray component and the measured temperature is likely to be an upper limit of the physical one.

We recall that an origin of the soft excess from a frequency-independent scattering is ruled out by present analysis (see § 4.1).

The interpretative scenario is however complex and no unambiguous interpretation can be claimed as a unique interpretation for the observational data. The results from future broadband missions (like *XTE* or *SAX*) will allow to determine with improved accuracy the parameters of all the spectral components involved and to constrain the possible models and their degrees of freedom.

## 6.5 Iron line

The *ASCA* AO2 observation of NGC4051 detected a clearly broad ( $\sigma \geq 0.2$  keV at 90% level of confidence) and complex emission line, that can be interpreted as a K-fluorescence iron line whose profile has been modified by gravitational and Doppler shifts. The profile and centroid of the line allow to derive quantitative constraints on the physical and geometrical properties of the emitting region. The emission complex observed can be characterized, according to the equations (1) to (3) in Matt *et al.* (1992a):  $E_{c\alpha} = 6.09 \pm 0.03$  keV,  $\sigma_{\alpha} = 418 \pm 16$  eV and  $EW_{\alpha} = 320 \pm 30$  eV (the results are the weighted mean of the parameters obtained applying the above equations to each detector continuum-subtracted spectrum). The emission is therefore: a) significantly redshifted ( $\sim 5\%$ ) in comparison to the expected energy for K-fluorescence emission line from neutral or mildly ionized iron; b) broad; c) particularly intense, being the average equivalent width of similar features observed in other Seyfert 1 galaxies  $\sim 150$  eV (Nandra & Pounds 1994). Tanaka *et al.* (1995) reported the discovery of an analogous complex emission feature in the 200,000 ks spectrum of the Seyfert 1 galaxy MGC-6-30-15, giving the first conclusive evidence of the effects due to the presence of a supermassive black hole in the proximity of the line radiation field. Explanations alternative to the relativistic accretion disk seem to be excluded for that object (Fabian *et al.* 1995). Nonetheless the correct interpretation is far from clear and some problems are left unsolved even if we consider only the NGC4051 results. Matt *et al.* (1992) showed the  $EW$  of a line emerging from an accretion disk can hardly exceed  $\sim 180$  eV, a value that is inconsistent with the observed  $EW \sim 270$  eV. An overabundance of iron of such order of magnitude could be a straightforward explanation for such discrepancy. Moreover, higher equivalent widths can be achieved if the matter in the accretion disk is highly ionized (Zycki & Czerny 1994) due to the increased fluorescence yield and the reduced photoelectric opacity;  $EW \sim 300$  eV can be achieved if the mean ionization state of iron is  $\sim \text{FeXXIII}$ . In such case the rest energy of the emitted line is expected to lie around  $\sim 6.7$  keV.

The quoted results allow to put some significant constraints on the iron line emission region. Following the fully relativistic treatment of Matt *et al.* (1992a, 1992b), the

observed centroid energy and intrinsic width of the line profile require an inner radius  $R_i \sim 10 R_S$ , with a comparable size of the nuclear source. The outer radius  $R_o$  cannot be tightly constrained, and might be as high as  $\sim 10^3 R_S$  if  $R_i$  could shrink to  $\sim 6 R_S$ . In case of a ionized disk,  $EW \sim 300 \text{ eV}$  can be obtained in the hypothesis of an extended source around a  $\sim 10^6 M_\odot$  black hole, provided a typical size of the source  $\sim 50 R_S$  and a sub-Eddington luminosity ( $L/L_{Edd} \simeq 0.5$ ) are achieved. In both cases the location of the innermost emitting region would lie in the range  $1 \div 5 \times 10^{12} \text{ cm}$ . Any response of the line to the variation of the nuclear continuum should lag at most  $\sim$  few hundreds of seconds. Incidentally, we remark that we have not detected any evidence of line variability in the NGC4051 observations, while recent measures claiming correlated iron-line/continuum variability in Seyfert 1 galaxies have recently appeared in literature (Iwasawa *et al.* 1996, Yaqoob *et al.* 1996).

Alternatively, a contribution to the line emission from a molecular torus surrounding the nucleus has been predicted by some authors (Krolik & Kallmann 1987, Ghisellini, Haardt & Matt 1994, Krolik, Madau & Zycki, 1994) and claimed as a possible explanation for the narrow line observed in the Seyfert 1 galaxy NGC7469 (Guainazzi *et al.* 1994, Leighly *et al.* 1995a). The line should be in such case narrow and centred at the nominal K-fluorescence energy for neutral iron (*i.e.*  $\simeq 6.40 \text{ keV}$ ). This explanation would fit well the multi-component structure of the iron line, that requires a narrow Gaussian line at the nominal  $K_\alpha$ -fluorescence energy superimposed to the relativistic double-horned profile, with  $EW \simeq 60 \text{ eV}$ . Such an intensity implies torus column density  $N_H \sim \text{few } 10^{23} \text{ cm}^{-2}$ , although much higher densities cannot be ruled out, since the  $EW$  value is only loosely constrained.

The discussion above is obviously affected by the choice of the self-consistent continuum and line model outlined. A confirmation of the sketched scenario with the upcoming broadband X-ray missions (*i.e.* *XTE* and *SAX*) is therefore strongly needed in order to achieve a deeper understanding of the physical process involved and of the relevant geometry.

## 7 Conclusions

The higher the resolution capabilities of the X-ray experiments, the more interesting and complex the emission of AGNs appears. The Seyfert 1 galaxy NGC4051 proves itself to be an outstanding target, that shares most of the peculiar characteristics of the objects of its class, and namely:

- a) strong variability on time scales as short as few hundreds seconds.
- b) Evidence of multicomponent X-ray spectrum, with an apparent soft excess emission superimposed on the higher energy power-law.
- c) Detection of absorption edges from ionized oxygen species and emission lines that represent clear evidence of warm absorbing matter along the line of sight.
- d) Variability constraints allow to locate the warm absorbing matter at a distance from the nuclear source  $\leq 10^{17} \text{ cm}$  with a numerical density  $n \geq 2 \times 10^{10} \text{ cm}^{-3}$ .
- e) the power-law spectral photon index is intrinsically variable (if reflection by a plane-parallel infinite disk is self-consistently supposed,  $\Delta\Gamma \sim 0.4$ )



- f) The iron line emission is redshifted, broad and very intense. The outcomes can be explained in terms of emission from a relativistic accretion disk, either cold with moderate inclination ( $\theta \sim 25^\circ$ ) or ionized and almost face-on. In the former case, the observed EW is higher by a factor  $\simeq 1.5 \div 2$  than the maximum allowed by presently available solar-abundance relativistic models. The puzzle of EW excess might be solved: *i*): postulating an *ad hoc* iron overabundance by a factor  $\simeq 1.5$ ; *ii*): if the reflection is from an ionized face-on disk; *iii*): if a contribution to the iron emission complex comes from the putative molecular torus surrounding the nucleus.

The evaluation of the above outlined results must take into account the peculiar properties of NGC4051, which is a low-mass ( $M_{bh} < 10^7 M_\odot$ ), low-luminosity ( $L_X \sim 10^{42} \text{ erg s}^{-1}$ ) and strongly X-ray variable (e-folding time  $\sim \text{few } 10^2 \text{ s}$ ) Seyfert 1. The mounting evidence for a positive correlation between the 2-10 keV flux and photon index point to an interpretation of the nuclear emission in terms of inverse Compton reprocessing of UV seed photons by a non-thermal distribution of relativistic electrons; the injected particles are likely to be generated in the immediate proximity of the putative black hole, while the exact location of the seed UV emitting region is still controversial.

NGC4051 exhibits all the main features often seen in Seyfert 1 X-ray spectra. The many peculiar features of this source (variable warm absorber, complex iron line structure, variable nonthermal continuum slope) allow a deeper insight on the general properties of physical processes in AGNs.

Although a further effort is needed for a full understanding of the complex interplay among the different spectral components and their dynamics (the contribution of broadband experiments will be of the primary importance to achieve such a goal), some interpretative milestones can be set: a non-thermal continuum, whose production mechanism requires an efficient and continuous injection of a non-thermal distribution of relativistic electrons, Compton reprocessing of the nuclear radiation, a complex absorber with an intrinsic warm component within the inner border of the BLR are the common elements any unified scenario must cope with.

## Acknowledgements

Valuable discussions with Massimo Cappi and Karen Leighly improved greatly the quality of this paper. The authors are deeply in debt with an anonymous referee for her/his detailed revision. M.G. acknowledges support by M.U.R.S.T. (Ministero dell'Università e della Ricerca Scientifica e Tecnologica).

## References

- Arnaud K.A. *et al.*, 1991, XSPEC User's Guide, ESA TM-09
- Band D.L., Klein R.I., Castor J.I. & Nash J.K., 1990, Ap.J., 362, 90
- Cavaliere A. & Morrison P., 1980, Ap.J., 238, L63
- Chakrabarti & Titarchuk, 1995, Ap.J., 455, 623
- Comastri A., Setti G., Zamorani G. & Hasinger G., 1995, Astron & Astrophys., 296, 1
- Dickey J.M. & Lockman F.J., 1990, Ann. Rev. Astron. & Astrophys., 28, 215
- Edelson R., 1992, Ap.J., 401, 516
- Fabian A.C., Nandra K., Reynolds C.S., Brandt W.N., Otani C., Tanaka Y., Inoue H., Iwasawa K., 1995, Mon. Not. R. Astron. Soc., *in press*
- Fabian A.C. & Rees M., 1979, in X-ray astronomy, Baity & Peterson eds., p.381
- Fabian A.C., Rees M.J., Stella L. & White N.E., 1989, Mon. Not. R. Astron. Soc., 238, 729
- Fabian A.C., Kunieda H., Inoue S., Matsuoka M., Mihara T., Miyamoto S., Otani C., Ricker G., Tanaka Y., Yamauchi M. & Yaqoob T., 1994, Publ. Astron. Soc. Jap., 46, L59
- Ferland G.J., 1991, Ohio State University, Astronomy Departement Internal Report 91-01
- Fiore F., Elvis M., Mathur S., Wilkes B.J. & McDowell J.C., 1993, Ap.J., 415, 129
- Fiore F., Perola G.C., Matsuoka M., Yamauchi M. & Piro L., 1992a, Astron. & Astrophys., 262, 37
- Fiore F., Perola G.C., Yamauchi M. & Matsuoka M., 1992b, in Proc. 28th Yamada Symposium on X-ray Astronomy, Nagoya, Japan, Tanaka Y. & Koyama K. eds., Tokyo:Universal Academy Press
- Gendreau K.C., Mushotsky R., Fabian A.C., Holt S.S., Kii T., Serlemijos P.J., Ogasaka Y., Tanaka Y. *et al.*, 1995, Publ. Astron. Soc. Jap., 47, L5
- George I.M. & Fabian A.C., 1991, Mon. Not. R. Astr. Soc., 249, 352
- George I.M., Turner T.J. & Netzer H., 1995, Ap. J. Lett., 438, L67
- Ghisellini G. & Haardt F., 1994, Ap.J.Lett, 429, L53
- Ghisellini G., Haardt F. & Matt G., 1994, Mon. Not. R. Astron. Soc., 267, 743
- Guainazzi M., Matsuoka M., Piro L., Mihara T. & Yamauchi M., 1994, Ap.J.Lett., 436, L35
- Guilbert P.W., Fabian A.C. & Rees M., 1983, Mon. Not. R. Astr. Soc., 205, 593
- Guilbert P.W. & Rees M.J., 1988, Mon. Not. R. Astr. Soc., 233, 475
- Huchra J. & Burg R., 1992, Ap.J., 393, 90
- Iwasawa K., Fabian A.C., Reynolds C.S., Nandra K., Otani C., Inoue H., Hayashida H., Brandt W.M., Dotani T., Kunieda H., Matsuoka M. & Tanaka Y., 1996, Mon. Not. R. Astron. Soc., *in press*
- Krolik J.H., & Kallmann T.R., 1987, Ap.J.Lett., 320, L5
- Krolik J.H., Kriss G.A., 1995, Ap.J., 447, 512
- Krolik J.H., Madau P. & Zycki P., 1994, Ap.J.Lett., 420, L57
- Krolik J.H., McKee, Tarter, 1981, Ap.J., 249, 422
- Kunieda H., Hayakawa S., Tawara Y., Koyama K., Tsuruta S., Leighly K., 1992, Ap.J., 384, 482
- Lampton M., Margon B. & Bowyer S., 1976, Ap. J., 208, 177
- Lawrence A., Watson M.G., Pounds K.A., Elvis M., 1985, Mon. Not. R. Astron. Soc.,

217, 685

- Leighly K., Kunieda H., Awaki H., Tsuruta S., 1995, *submitted to Ap.J.*
- Leighly K., Mushotzky R., Yaqoob T., Kunieda H. & Edelson R., 1996, *in press*
- Liedhal D.A., Kahn S.M., Osterheld A.L. & Goldstein W.H., 1990, *Ap.J.*, 350, L37
- Lightman A.P. & White T.R., 1988, *Ap.J.*, 335, 57
- Marshall F.E., Holt S.S., Mushotzky R.F., Becker R.H., 1983, *Ap.J.Lett.*, 269, L31
- Matsuoka M., Yamauchi M. & Piro L., 1989, in *Proc. 23rd ESLAB Symposium*, Hunt J. & Battrick B. eds., ESA SP-296, pag.985
- Matsuoka M., Piro L., Yamauchi M., Murakami T., 1990, *Ap.J.*, 361, 440
- Matt G., Perola G.C. & Piro L., 1991, *Astron. & Astrophys.*, 247, 25
- Matt G., Perola G.C., Piro L. & Stella L., 1992a, *Astron. & Astrophys.*, 257, 63
- Matt G., Perola G.C., Piro L. & Stella L., 1992b, *Astron. & Astrophys.*, 263, 453
- McHardy I.M., Green A.R., Done C., Punchnarewicz E.M., Mason K.O., Branduardi-Raymond G. & Jones M.H., 1995, *Mon. Not. R. Astron. Soc.*, 273, 549
- Mihara T., Matusoka M., Mushotzky R.F., Kunieda H., Otani C., Miyamoto S., Yamauchi M., 1994, *Pub. Astron. Soc. Jap.*, 46, L137 (Paper I)
- Mushotzky R.F., Fabian A.C., Iwasawa K., Kunieda H., Matsuoka M., Nandra K., & Tanaka Y., 1995, *Mon. Not. R. Astron. Soc.*, 272, L9
- Nandra K. & Pounds K.A., 1994, *Mon. Not. R. Astron. Soc.*, 268, 405
- Netzer H., 1993, *Ap.J.*, 411, 594
- Netzer H., Turner T.J., George I.M., 1994, *Ap.J.*, 435, 106
- Osterbrock D.E., Martel A., 1993, *Ap.J.*, 414, 552
- Otani C., 1996, *Ph.D. thesis*, Tokyo University
- Otani C., Kii T., Reynolds C.S., Fabian A.C., Iwasawa K., Hayashida K., Inoue H., Kunieda H., Makino F., Matusoka M., Tanaka Y., 1996, *Publ. Astron. Soc. Jap.*, 48, 211
- Otani C., & Dotani T., 1994, *Asca News* n.2, 25
- Pounds K.A., Nandra K., Fink H.H., Makino F., 1994, *Mon. Not. R. Astron. Soc.*, 267, 193
- Ptak A., Yaqoob T., Serlemitsos P.J. & Mushotzky R.F., 1994, *Ap. J. Lett.*, 436, L31
- Reynolds C.S. & Fabian A.C., 1995, *Mon. Not. R. Astron. Soc.*, 273, 1167
- Reynolds C.S., Fabian A.C., Nandra K., Inoue H., Kunieda H. & Iwasawa K., 1995, *Mon. Not. R. Astron. Soc.*, *in press*
- Rybicki G.B. & Lightman A.P., 1979, *Radiative processes in astrophysics*, New York:John Wiley & Sons
- Svensson R., 1994, *Ap.J. Suppl. Ser.*, 92, 585
- Tanaka Y., Inoue H., & Holt S.S., 1994, *Publ. Astron. Soc. Jap.*, 46, L37
- Tanaka Y., Nandra K., Fabian A.C., Inoue H., Otani C., Dotani T., Hayashida K., Iwasawa K. *et al.*, 1995, *Nature*, 375, 659
- Torricelli-Ciamponi G. & Courvoisier T. J.-L., 1995, *Astron. & Astrophys.*, 296, 651
- Turner T.J., Weaver K.A., Mushotzky R.F., Holt S.S. & Madjeski G.M., 1991. *Ap.J.*, 381, 85
- Urry C.M., Arnaud K., Edelson R.A., Kruper J.S. & Mushotzky R.F., 1989, in *AGN and X-ray background*, *Proc.32nd ESLAB Symposium*, Vol.2, Hunt J. & Battrick B. eds., ESA, SP-296, p.789
- Yaqoob T., 1990, *Ph.D. thesis*, University of Leicester
- Yaqoob T., 1992, *Mon. Not. R. Astron. Soc.*, 258, 198

Yaqoob T., Edelson R., Weaver K.W., Warwick R., Mushotzky R.F. Serlemijos P.J. &  
 Holt S.S., 1995, Ap. J., 453, 81  
 Yaqoob T., Serlemijos P.J., Turner T.J., George I.M., Nandra K., 1996, Ap.J.Lett., *in  
 press*  
 Yaqoob T. & Warwick R., 1991, Mon. Not. R. Astron. Soc., 248, 773  
 Yaqoob T., Warwick R., Makino F. *et al.*, 1993 Mon. Not R. Astron. Soc., 262, 435  
 Zycki P.T. & Czerny B., 1994, Mon. Not. R. Astron. Soc., 266, 653

## Figure captions

**Figure 1.** Broadband SIS0 and GIS2 light curves with binning time  $\Delta t = 312.5$  s. Time is expressed in seconds starting from the beginning of the observation.

**Figure 2.** Distribution function of the lowest doubling times for the broad band curves of Figure 1 ( $\Delta t = 100$  s). The distribution functions have been fit with an empirical equation of the form:  $A[1 - \exp(-\Delta t/\tau)]$ . Best-fit values are:  $\tau_{SIS0} = 500 \pm 300$  s and  $\tau_{GIS2} = 400 \pm 300$  s.

**Figure 3.** Broadband spectra (*upper panels*) and residuals in units of  $\sigma$  (*lower panels*) when a simple power-law with cold absorption is applied. The energy channels have been rebinned in order to have a S/N ratio  $\geq 25$ . Soft excess below  $E \sim 1$  keV and a broad emission line feature around  $E \sim 6.1$  keV are clearly visible.

**Figure 4.** Data/model ratio when a CLOUDY “warm absorber” model is applied to the SIS0+1 data. Bad modelling of the OVII edge and a prominent emission-like feature at energy  $E \sim 0.95$  keV are clearly seen.

**Figure 5.** Data/model ratio for a simple power-law model applied to the SIS0 and SIS1 spectrum in the energy range [3-10 keV]. The energy channel have been rebinned in order to have a S/N ratio  $\geq 15$ . In the upper panel a centroid energy vs. Gaussian dispersion contour plot is shown for the emission complex main component when the power-law + flat reflection + emission complex model is applied to the spectra of all detectors simultaneously. The outermost contour corresponds to 90% level of confidence for two interesting parameters ( $\Delta\chi^2 = 4.61$ ). At such level of confidence the line is broad ( $\sigma \geq 0.2$  keV).

**Figure 6.** PHA ratio between the HS and LS phase SIS0 spectra (definition of intensity phases is given in text).

**Figure 7.** [2.5-5.0 keV] and [0.7-1.3 keV] bands and SR SIS0+1 light curves for a binning time  $\Delta t = 500$  s.

**Figure 8.** SR vs. [0.7-5 keV] count rate for the SIS0+1 light curve with binning time  $\Delta t = 5000$  s. The reduced  $\chi^2$  for constant hypothesis is 8.9 and the linear correlation coefficient for 29 degrees of freedom  $r_{29} = 0.71 \pm 0.07$ .

**Figure 9.** OVII edge energy vs. optical depth contour plot for High State (HS), Low State subtracted of the 10th orbit (LS\*) and 10th orbit. The 10th orbit coincides with the  $\sim 2 \times 10^4$  s interval when the source flux is minimum. The outermost contour corresponds to the 99% level of confidence for two interesting parameters ( $\Delta\chi^2 = 9.21$ ). The definition of the intensity phases is given in text.

**Figure 10.** The same as Figure 10 for OVIII.

**Figure 11.** The same as Figure 9 when a model similar to Model “L” is applied but a bremsstrahlung (*left panel*) or power-law (*right panel*) emission model is substituted for the blackbody.

**Figure 12.** Photon index vs. [2–10 keV] luminosity for both AO2 and PV phase data (indicated by an arrow).